

# Bifurcation study for a surface-acoustic-wave driven meniscus

Kevin David Joachim Mitas,<sup>1,\*</sup> Ofer Manor,<sup>2</sup> and Uwe Thiele<sup>1,3,†</sup>

<sup>1</sup>*Institut für Theoretische Physik, Westfälische Wilhelms-Universität Münster,*

*Wilhelm Klemm Str. 9, 48149 Münster, Germany*

<sup>2</sup>*Wolfson Department of Chemical Engineering,*

*Technion - Israel Institute of Technology, Haifa, Israel 32000<sup>‡</sup>*

<sup>3</sup>*Center of Nonlinear Science (CeNoS),*

*Westfälische Wilhelms-Universität Münster,*

*Corrensstr. 2, 48149 Münster, Germany*

## Abstract

A thin-film model for a meniscus driven by Rayleigh surface acoustic waves (SAW) is analysed, a problem closely related to the classical Landau-Levich or dragged-film problem where a plate is withdrawn at constant speed from a bath. We consider a mesoscopic hydrodynamic model for a partially wetting liquid, where wettability is incorporated via a Derjaguin (or disjoining) pressure and combine SAW driving with the elements known from the dragged-film problem. For a one-dimensional substrate, i.e., neglecting transversal perturbations, we employ numerical path continuation to investigate in detail how the various occurring steady and time-periodic states depend on relevant control parameters like the Weber number and SAW strength. The bifurcation structure related to qualitative transitions caused by the SAW is analysed with particular attention on the Hopf bifurcations related to the emergence of time-periodic states corresponding to the regular shedding of lines from the meniscus. The interplay of several of these bifurcations is investigated obtaining information relevant to the entire class of dragged-film problems.

---

\*Electronic address: [kevin.mitas@uni-muenster.de](mailto:kevin.mitas@uni-muenster.de)

†Electronic address: [u.thiele@uni-muenster.de](mailto:u.thiele@uni-muenster.de); URL: <http://www.uwethiele.de>; ORCID ID: 0000-0001-7989-9271

‡Electronic address: [manoro@technion.ac.il](mailto:manoro@technion.ac.il)

## I. INTRO

Over recent years, the interest of industry has grown in applications that control the deposition of a surface coating via the transfer of simple or complex liquids from a bath. Examples are dip-coating processes and Langmuir-Blodgett transfer processes of liquids, solutions and suspensions [23, 27, 40, 56, 71, 72].

The transfer of a simple viscous liquid from a bath onto a continuously withdrawn plate is an important reference case for all investigations of coating phenomena. Where the bath contacts the plate, a dynamic liquid meniscus is formed resulting from the acting forces of capillarity due to surface tension, the viscous drag force of the liquid advection and the wettability of the plate. The latter results from the interaction of the liquid, the solid and the ambient gas at the three-phase contact line. Overall, this phenomena is known as the Landau-Levich problem as it was first theoretically analysed by Landau and Levich [33] and Derjaguin [17] in the case of a simple ideally wetting nonvolatile liquid. They show, that a homogeneous macroscopic liquid layer is deposited on the plate whose thickness  $h_c$  depends on the capillary number  $Ca = \mu v_p / \gamma$  in the form of a power law,  $h_c \propto Ca^{2/3}$ . Here,  $v_p$  is the velocity of the plate withdrawal, and  $\mu$  and  $\gamma$  are the viscosity and surface tension of the liquid, respectively. For partially wetting liquids, a transition from a meniscus state where a macroscopically dry plate emerges from the bath to the Landau-Levich regime occurs at a finite plate velocity [22, 23, 56, 75]. Several different modi of transition are described and are classified as dynamic unbinding transitions [22]. In the course of these transitions beside meniscus states and Landau-Levich states, so-called foot states may occur, where a steady finite-length foot-like protrusion covers part of the moving plate [22, 23, 56, 75]. Time-periodic states corresponding to the periodic shedding of liquid ridges, oriented orthogonally to the withdrawal direction, from the liquid meniscus are also described [59], similar to line deposition occurring in Langmuir-Blodgett transfer [28–30]. Here, we refer to this phenomenon as line deposition.

The classic Landau-Levich or dragged-plate system is a prominent example of a wide class of related coating systems where a meniscus deforms and film deposition occurs under lateral driving forces. For instance, plate withdrawal may be replaced by a temperature gradient along the plate [8, 10, 12, 14, 45, 46, 55], by a pressure gradient when propelling an air bubble through a tube (Landau-Levich-Bretherton problem) [11, 31] and by Rayleigh surface acoustic waves (SAWs), which propagate in a resting plate in contact with a bath of liquid. Here, we are particularly

interested in the latter.

Briefly, simple vibrations, flexural bulk waves, and Rayleigh surface acoustic waves (SAWs) in solid substrates are capable of displacing, manipulating, and deforming liquid films and drops [5, 9, 44]. In particular, Rayleigh type SAWs, which are of MHz frequency and propagate in a solid substrate, cause the dynamic wetting of the solid surface by liquid films. This was first shown by Rezk et al. [52, 53] for the case of silicon oil. They named the phenomenon *acoustowetting* that was thoroughly explained in a later study [3]. Similar observations are made in the case of water, albeit there capillary stresses compete with and even diminish the SAW induced dynamic wetting effect [4, 41]. Generally, the direction of the SAW-induced dynamic wetting is determined by the thickness of the liquid film and the wavelength of the SAW. This is consistent with an interplay between radiation pressure and acoustic flow in oil films. Liquid film thicknesses, which are small with respect to the wavelength of sound leakage off the SAW, dynamically wet the solid substrate along the propagation direction of the SAW. The wavelength of the sound leakage is approximately the wavelength of the SAW times the ratio between the phase velocities of the SAW and of sound in the liquid and is in the range of tens to hundreds of microns in the case of MHz-frequency SAWs. In case the thickness of the liquid film is comparable to the wavelength of the sound leakage, acoustic resonance effects were found to enhance the pressure in the liquid film, so that the film may also spread opposite to the direction of the Rayleigh SAW. In addition, when the thickness of the liquid film is greater than a few wavelengths of the sound leakage, a different mechanism, Eckart streaming, was found to govern transport in the liquid, yielding again dynamic wetting along the direction of the SAW. The capillary stress at the free liquid surface is capable of arresting the dynamic wetting of the liquid film, especially in the case of water. The opposite contributions of capillary and SAW to film dynamics is quantitatively weighed in an acoustic Webber number, which predicts the onset of dynamic wetting and is further discussed in this paper.

Results obtained for these Landau-Levich-type systems are also of relevance for other possibly more complicated coating geometries [13, 71, 73] and also provide a basis for the understanding of the behaviour of more complex liquids in similar settings [1, 6, 15, 51, 54, 62, 72]. Often, Landau-Levich-type systems are modelled based on mesoscopic hydrodynamic thin-film models (also called long-wave or lubrication models) [15, 47]. It is assumed that length scales orthogonal to the substrate are small compared to the ones parallel to the substrate, e.g., cases of small contact angles and small interface slopes. This allows for the derivation of an evolution equation for the

film thickness profile. Thereby the motion of three-phase contact lines is either modeled through a slip model [56, 75] or a precursor film model [22, 59]. Here, we employ the latter, i.e., wettability is modelled by an additional pressure term, the so-called Derjaguin (or disjoining) pressure that allows for an ultrathin adsorption layer on the macroscopically dry substrate [16, 18, 58, 60].

Employing such a precursor film model, Ref. [22] showed that depending on plate inclination angle (and equilibrium contact angle), different transition scenarios occur with increasing capillary number (dimensional plate velocity). These are, in particular, four different continuous and discontinuous unbinding (or dynamic wetting and emptying) transitions that are out-of-equilibrium equivalents of equilibrium transitions, which were discussed earlier (see [22] and references therein).

Here, we consider how the picture is amended when employing SAW driving to force the meniscus instead of driving by dragging a plate. SAW driving for this purpose was recently investigated experimentally and theoretically [3, 4, 41–43, 52, 53]. In this system, a drop of liquid or liquid meniscus rests on a smooth solid plate. Then a propagating SAW is excited in the plate. The SAW is a propagating vibration in the substrate in the MHz-frequency range and may induce drops to slide, static menisci to deform and a liquid protrusion or film to spread from a static meniscus. Among other mechanisms, this is caused by a high-frequency periodic flow in a boundary layer close to the substrate within the liquid that induces a mean convective flow on hydrodynamic length and time scales. This flow may overcome the capillary and wettability resistance in the contact line region where the meniscus meets the plate, so that at a critical strength, the acoustically driven flow results in an advance of the contact line. This is very similar to the transitions, which occurs at critical capillary numbers in the Landau-Levich problem for partially wetting liquids. It remains an open question whether SAW driving can be employed to control deposition of structured coatings, which may be a simpler coating technique with no moving parts, compared to driving the coating film by moving the plate [38, 42].

In particular, here we combine the precursor-based thin-film model for the Landau-Levich problem for partially wetting liquids in Refs. [22, 59, 67] with the thin-film model for the SAW-driven meniscus in Ref. [43]. With other words, the SAW-model of [43] is expanded by introducing lateral forces due to the withdrawal of an inclined plate and substrate wettability. This allows us to investigate the behavior of the SAW-driven system in direct comparison to results obtained for the dragged-plate system. The model is numerically investigated employing a combination of path continuation techniques [2, 19, 20] bundled in the software package PDE2PATH [68, 70] and direct time simulation provided by the software package OOMPH-LIB [25].

We consider a one-dimensional substrate, i.e., we neglect transversal perturbations, and investigate in detail how the various occurring steady and time-periodic states depend on relevant control parameters like the Weber number and SAW strength. We uncover the full bifurcation structure related to qualitative transitions caused by the SAW. We pay particular attention to Hopf bifurcations, which bring about the emergence of time-periodic states corresponding to the regular shedding of lines from the meniscus. The interplay of several of these bifurcations is investigated by tracking the bifurcations in selected parameter planes, thereby discussing the special transition points (so called codimension-2 bifurcations) where the individual bifurcations emerge and disappear. Our study gives detailed information which is relevant to the entire class of dragged-film problems.

The structure of our work is as follows: In section II, we briefly introduce the governing mathematical model, provide a short overview of the employed continuation method, and discuss the used solution measures. Next, we reproduce selected bifurcation diagrams for the classical Landau-Levich system [22] in section III and produce, in comparison, bifurcation diagrams for the SAW-driven case [43] in section IV A. The comparison provides us with central reference cases for our study. In continuation, in section IV B the results of [43] for steady states are extended towards partially wetting liquids. The obtained bifurcation diagrams show a number of Hopf bifurcations. Their behavior is analyzed in detail in section IV C together with properties of the emerging branches of stable and unstable time-periodic states. Finally, we conclude in section V with a summary and outlook.

## II. MODEL

In our study we combine the two systems sketched in Fig. 1, namely, a simple nonvolatile partially wetting liquid in the classical dip-coating (or Landau-Levich) geometry [22, 59] and a liquid meniscus driven by surface acoustic waves (SAW) [43]. Overall the set-up for the two systems is very similar with the main difference beside the driving force being the condition on the bath/meniscus side. The kinetic equation that describes the development of the film thickness profile  $h(x, t)$  when the two systems are combined reads in nondimensional form in the case of a one-dimensional substrate

$$\partial_t h(x, t) = -\partial_x \left\{ Q(h) \partial_x \left[ \frac{1}{\text{We}_s} \partial_{xx} h - f'(h) \right] - \chi(h) + h [\epsilon_s v_s(h) + U_0] \right\}, \quad (1)$$

where  $\chi(h) = G Q(h) (\partial_x h - \alpha)$ ,  $Q(h) = \frac{h^3}{3}$ .

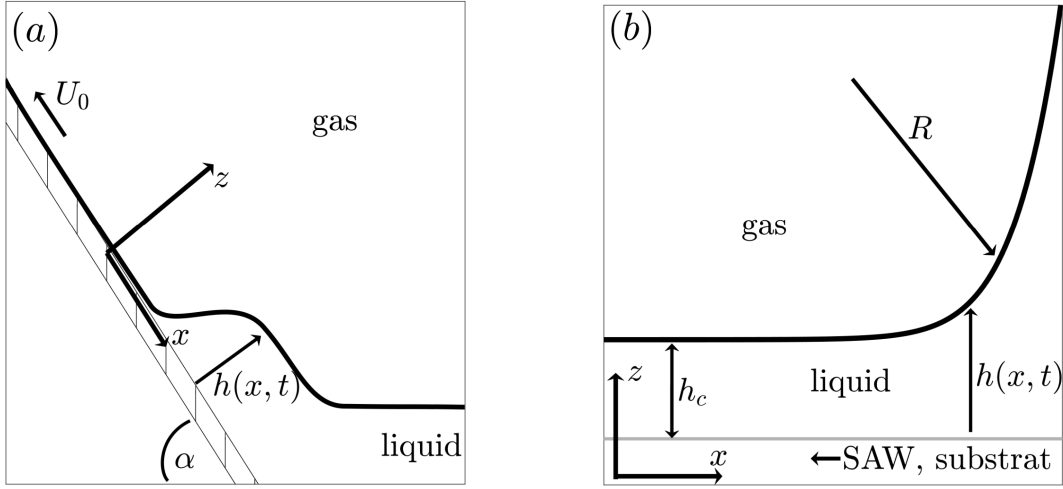


FIG. 1: Sketches of the meniscus regions of the systems in consideration: (a) a Landau-Levich-type coating system, where liquid is deposited on a plate, which is withdrawn at an angle  $\alpha$  from a liquid bath at a velocity of  $U_0$ ; (b) a Landau-Levich-type coating system, where liquid is deposited on a plate from a liquid meniscus with radius of curvature  $R$  onto a horizontal plate, which supports a surface acoustic wave (SAW).

Above,  $\alpha$  is the substrate inclination angle in long-wave scaling,  $Q(h)$  is the mobility function resulting from a no-slip boundary condition at the substrate,  $We_s$  is the Weber number, and  $G$  is a dimensionless gravity number. The wetting potential [50, 61]

$$f(h) = Ha \left( \frac{h_p^3}{5h^5} - \frac{1}{2h^2} \right) \quad (2)$$

describes wettability for a partially wetting liquid and results in the Derjaguin (or disjoining) pressure  $\Pi = -f'(h) = Ha(h_p^3/h^6 - 1/h^3)$  [58, 61].  $Ha$  is a nondimensional Hamaker number that controls the long-wave equilibrium contact angle.

In addition, capillarity and wettability give rise to the Laplace and Derjaguin pressure contributions in the first bracket of Eq. (1). The next term  $[\chi(h)]$  accounts for gravitational contributions that balance for the bath where  $\partial_x h = \alpha$  and the final bracket gives the driving force for the coating process. It combines the effect of the plate moving at a velocity  $U_0$  and of the SAW at an intensity of  $\epsilon_s$ . The corresponding dependence of SAW-driving on the thickness of the liquid films is [43]

$$v_s(h) = \frac{1}{4h} \left( \frac{h \sinh(2h) - h \sin(2h) + 2 \cosh(h) \cosh(h)}{\cos(2h) + \cosh(2h)} - 1 \right), \quad (3)$$

which is illustrated in Fig. 2. The influence of the SAW on the coating process increases with

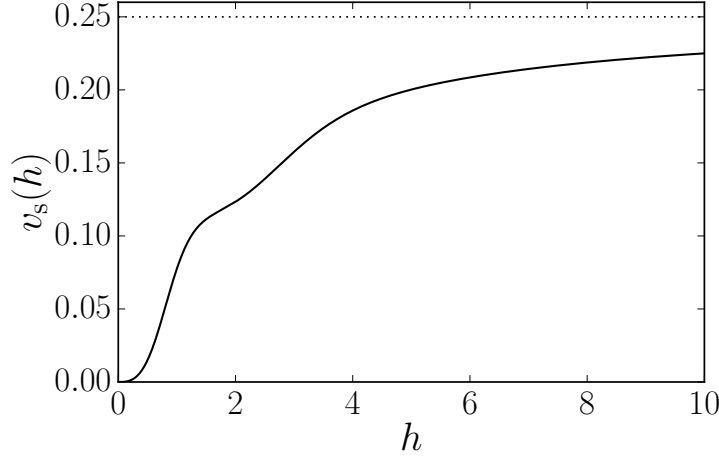


FIG. 2: Dependence of the average velocity in the liquid film,  $v_s$ , on film thickness  $h$  (solid line). The thin horizontal dotted line corresponds to the asymptotic value of  $v_s = 1/4$  at large  $h$ .

increasing film thickness and saturates in the limit of large film heights.

The employed scaling allows us to use both, the Weber number  $We_s$  and the SAW strength  $\epsilon_s$ , as control parameters. This facilitates comparison to Ref. [43] where  $We_s$  is the control parameter and also to [22, 59] where the the nondimensional velocity of the dragging plate is used – a parameter that has a similar role as  $\epsilon_s$  for the SAW-driving. The scaling is discussed in detail in the Appendix A and combines aspects of the scalings employed in Refs. [43] and [22, 59].

Equation (1) is derived using the well-established lubrication approximation, which is also known as long-wave or thin-film approximation [15, 47, 60], i.e., it is assumed that all relevant length scales orthogonal to the substrate are small compared to the ones parallel to the substrate, e.g., one considers the case of small contact angle, small plate inclination angle and, in general, small interface slopes.

The particular combination of dragged-plate driving and SAW-driving has to our knowledge not yet been treated in the literature. The derivation starts from the Navier-Stokes and continuity equations with the usual stress-free conditions at the free surface of the liquid film and with no-slip and no-penetration conditions at the solid-liquid interface. In addition, the solid-liquid interface undergoes SAW-induced high-frequency travelling wave oscillations. This implies that fast and slow time-scales have to be separated in a multi-scale approach that then results in the particular effective SAW-driving term  $v_s$  that acts on the viscous time scale [3, 4, 43]. A similar approach is employed for liquid films on vertically vibrated substrates where it is used to stabilize various

interface instabilities [34, 65].

The resulting Eq. (1) allows us to investigate the different limiting cases studied in the literature:

- (i) The model in Ref. [43] is recovered without wettability ( $f = 0$ ) and without gravity ( $G = 0$ ).
- (ii) The model in Refs. [22, 59] is recovered without SAW-driving ( $\epsilon_s$ ).

We set specific boundary conditions (BC) for  $h(x, t)$  to investigate the dragged-plate and SAW-driven coating system. We consider the domain  $\Omega = [-L/2, L/2]$ , where

$$\begin{aligned} h &= h_m, \quad \text{and} \quad \partial_{xx}h = 1 \quad \text{at} \quad x = L/2 \\ \partial_x h &= 0 \quad \text{and} \quad \partial_{xx}h = 0 \quad \text{at} \quad x = -L/2 \end{aligned} \tag{4}$$

i.e., on the meniscus side ( $x = L/2$ ) the film profile approaches a meniscus of constant curvature exactly as in Ref. [43]. Note that the nondimensional radius of curvature is equal to one. For the dragged-plate system this BC is amended to  $\partial_{xx}h|_{x=L/2} = 0$  as the profile approaches a straight line. The other BC on the bath/meniscus side fixes the film thickness on the boundary of the numerical domain to  $h_m$ , this essentially pins the translational degree of freedom and controls the position of the contact line region within the numerical domain. The BC on the opposite side ( $x = -L/2$ ) allow for a flat film of arbitrary  $h_c$  – the coating height. These boundary conditions set the necessary conditions to solve Eq. (1). We numerically investigate the model Eq. (1) with the introduced BC by employing a combination of pseudo-arclength path continuation [2, 19, 20] as bundled in PDE2PATH [68, 70] and direct time simulations using OOMPH-LIB [25].

Briefly, the pseudo-arclength path continuation technique is employed to determine steady solutions ( $\partial_t \phi = 0$ ) of Eq. (1). This is written as the operator  $G[\phi, \lambda] = 0$ , which is discretized using a finite element scheme. Here,  $\lambda$  stands for a control parameter or a set of them. One follows a discretized solution  $\phi(x)$  in parameter space varying  $\lambda$  using a prediction-correction scheme: in the prediction step, one uses the tangent of the solution curve to advance from the known solution at parameter value  $\lambda$  to a first guess of a solution at a new parameter value  $\lambda + \Delta\lambda$ , i.e., the control parameter is used as continuation parameter. Then, in the correction step a Newton procedure is employed to converge from the guess to a solution of the PDE at  $\lambda + \Delta\lambda$ . This procedure is iterated to advance step by step along a solution branch. However this simple continuation scheme fails when the solution branch undergoes a saddle-node bifurcation (or fold). Therefore one employs pseudo-arclength continuation, where the arclength  $\Delta s$  along the branch is employed as continuation parameter while the original control parameter  $\lambda$  is in the correction step adjusted at fixed  $\Delta s$  in parallel to the state  $\phi$ . The arclength  $\Delta s$  itself is determined through an approximation, hence



the name “pseudo-arclength continuation”. This allows one to follow solution branches through saddle-node bifurcations. The package also allows to detect various bifurcations, track them in parameter planes through tow-parameter continuations, switch to bifurcating branches of other steady states or to branches of time-periodic states [68–70]. For other recent examples where path continuation is applied to thin-film and closely related equations see [20, 21, 30, 35, 36, 59, 64, 66]. Here, we used continuation to investigate in detail how the various occurring steady and time-periodic states depend on relevant control parameters like the Weber number and SAW strength. The results are presented in terms of bifurcation diagrams employing as main solution measures (i) the thickness of the coating layer, i.e., the value of  $h$  measured on the boundary at  $x = -L/2$ , and (ii) the excess volume  $V_{\text{ex}} = V - V_0$  of liquid dynamically extracted from the bath/meniscus. The volume is calculated as the integral  $V = \int_{\Omega} h(x)dx$  and  $V_0$  is the reference volume without driving. In the case of time periodic states the mean value of the measure over one period is shown and the period is used as an additional solution measure.

### III. DRAGGED FILM WITHOUT SAW

Before we present our main results for the SAW-driven case, we first give an overview of the transitions occurring for the classical Landau-Levich system [22, 56, 75]. Employing Eq. (1) with  $We_s = 1$ ,  $Ha = 1$  and  $\epsilon_s = 0$ , we obtain the thin-film equation analysed in [22] with only a small change in the boundary conditions as discussed in the final part of section II. As explained in the Appendix A [case (i)], this setting is equivalent to the scaling employed in [22, 59]. The remaining main control parameters are the plate velocity  $U_0$  and inclination angle  $\alpha$ . The geometry is as given in Fig. 1 (a). The bifurcation diagrams in the four main panels of Fig. 3 indicate how the dependence of the meniscus state on  $U_0$  changes with increasing  $\alpha$ . The insets give a selection of particular steady stable and unstable profiles.

In all cases, for  $U_0 \rightarrow 0$  the steady meniscus approaches the reference state of zero excess volume. The profile shows a smooth continuous transition from the bath to the coating layer of thickness  $h_c$ . It corresponds to the adsorption layer of equilibrium thickness  $h_c = h_p = 1$  given by  $\Pi(h) = 0$ . The behaviour for increasing  $U_0$  qualitatively depends on the value of  $\alpha$ : Fig. 3 (a) shows that at small  $\alpha$ , the excess volume  $V_{\text{ex}}$  monotonically increases with  $U_0$ , first slowly than faster until it diverges at a critical value  $U_{c1} \approx 0.021$  of the velocity at  $U_0$ . All states on the branch are linearly stable. The steady meniscus profile deforms as the velocity increases and a foot-like structure of

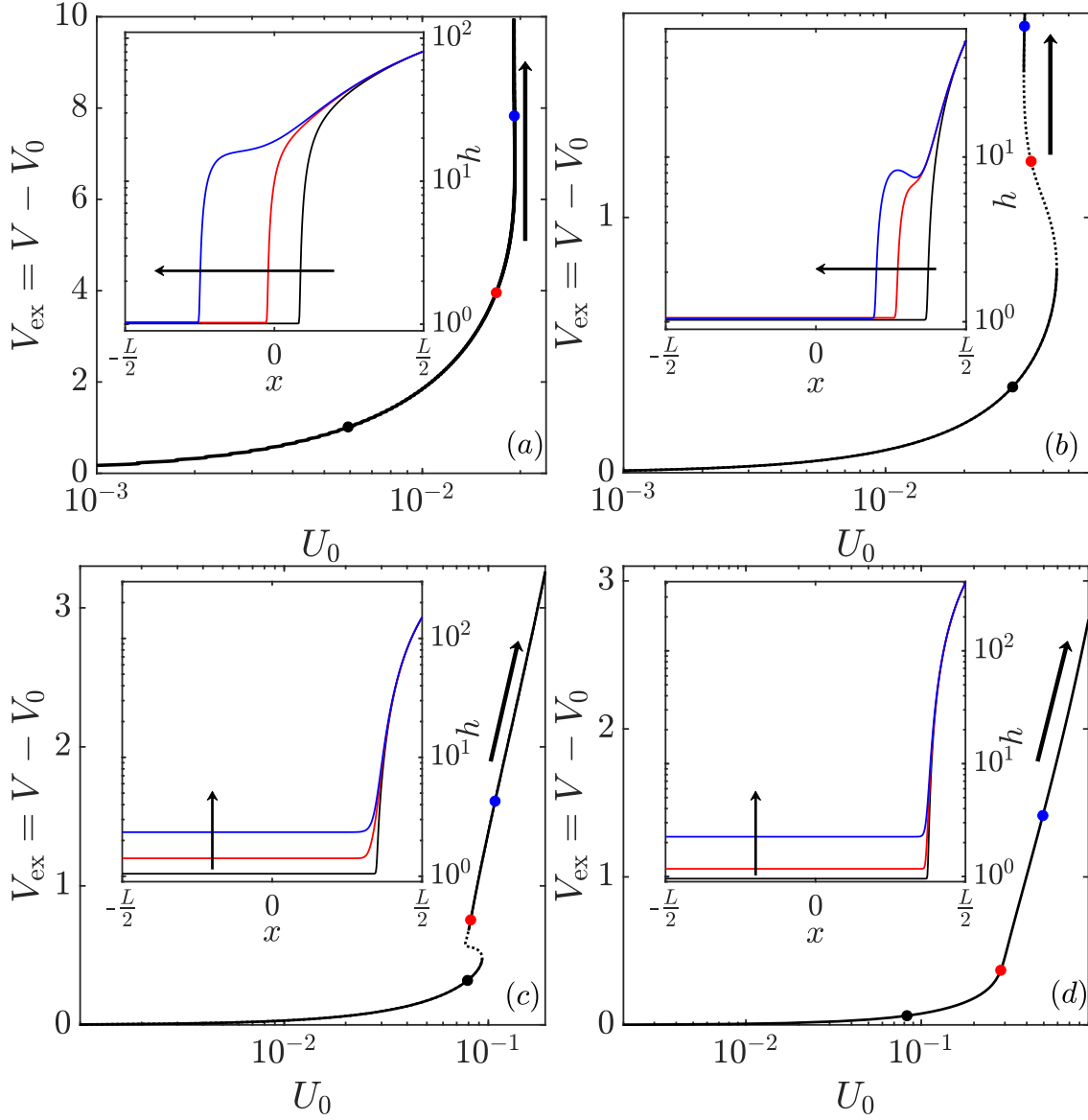


FIG. 3: Bifurcation diagrams of steady meniscus states in dependence of plate velocity  $U_0$  for the classical Landau-Levich system at different inclination angles (a)  $\alpha = 0.2$ , (b)  $\alpha = 1.0$ , (c)  $\alpha = 3.0$  and (d)  $\alpha = 10.0$  [Eq. (1)]. The shown solution measure is the excess volume  $V_{\text{ex}} = V - V_0$ . The dotted and solid lines represent unstable and stable states, respectively. Examples of steady state profiles are shown in the insets at loci indicated on the bifurcation curves by correspondingly coloured, filled circles. Note that the thickness scale is logarithmic. The arrows along the bifurcation curves and in the insets indicate corresponding directions of change. The remaining parameters are  $\text{Ha} = 1.0$ ,  $\text{We}_s = 1.0$ ,  $G = 0.001$ ,  $h_p = 1$ ,  $\epsilon_s = 0$ , and  $L = 800$ .

increasing length is dragged out from the bath with its length diverging for  $U_0 \rightarrow U_{c1}$  (see inset of Fig. 3 (a)). For  $U_0 > U_{c1}$ , time simulations show that a foot is continuously drawn out of the bath, and the system eventually settles on a Landau-Levich film state (not shown here). The transition at  $U_{c1}$  is termed “dynamic continuous emptying transition” [22] in analogy to the equilibrium emptying transition described in [48].

The first qualitative change in the bifurcation curve occurs at  $\alpha = \alpha_{c1} \approx 0.5$ , see Fig. 3 (b) for an example of a diagram at  $\alpha = 1.0 > \alpha_{c1}$ . At small  $U_0$  the excess volume monotonically increases with  $U_0$  as before, however, then at  $U_0 \approx 0.5$  a saddle-node bifurcation occurs and the bifurcation curve continues towards smaller  $U_0$  now consisting of unstable states. At a second saddle-node bifurcation at  $U_0 \approx 0.3$  the states become stable again, and the curve folds back towards larger  $U_0$ . Overall the curve undergoes an exponential (or collapsed) snaking [39] about a vertical asymptote at a critical velocity  $U_0 = U_{c2} \approx 0.3$ . We emphasize that at each fold there occurs a change in stability. This is analysed in detail in [67]. Looking at the inset of Fig. 3 (b), the steady profiles again develop a foot whose span now shows undulations. This is related to the snaking bifurcation curve and the fact that only certain ranges of foot length correspond to stable states. The transition at  $U_0 = U_{c2}$  is termed “dynamic discontinuous emptying transition” [22]. Note, that qualitatively our results agree with the ones of [22], although slightly different BC and domain sizes result in different critical values.

The second qualitative change in the bifurcation curve occurs at  $\alpha = \alpha_{c2} \approx 2.52$ , see Fig. 3 (c) for an example at  $\alpha = 3.0 > \alpha_{c2}$ . At small  $U_0$  the curve behaves as before, then undergoes a single pair of saddle-node bifurcations; both destabilize the states, i.e., two eigenvalues have positive real parts after the second one. At further increased  $U_0$ , the steady states become stable again at a Hopf bifurcation, where two complex conjugated eigenvalues cross the imaginary axis. This bifurcation was only recently described in Ref. [59] and is discussed in detail for the SAW-driven system in section IV C. The branch of stable states continues to arbitrarily large  $U_0$  following the classical Landau-Levich power law  $V_{\text{ex}} \propto U_0^{2/3}$ . Note that in contrast to the cases shown in Fig. 3 (a) and (b), no asymptotic value of  $U_0$  is found. Inspecting the steady profiles in the inset of Fig. 3 (c) shows that the transition does not involve an advancing foot. Instead, the coating thickness  $h_c$  increases homogeneously. As the film surface after “unbinding” from the substrate homogeneously increases similar to an equilibrium wetting transition, the transition is called a “discontinuous dynamic wetting transition” [22].

The final qualitative change in the bifurcation curve can be appreciated when comparing Fig. 3 (c)

and Fig. 3 (d). In Fig. 3 (d) the pair of bifurcations has annihilated and the curve increases monotonically. Otherwise the behaviour is as in Fig. 3 (c) - also see the profiles in the inset. In consequence, this behaviour is termed “continuous dynamic wetting transition” [22].

This brief overview of the classical Landau-Levich system in the case of partially wetting liquid provides the reference case that we compare to the SAW-driven meniscus, which we consider next.

#### IV. SAW-DRIVEN MENISCUS

After the brief revision of the transition behaviour in the case of the well-studied Landau-Levich system that serves as our reference system, we next consider the SAW-driven system. First, we investigate in section IV A the influence of the Weber number that is the main control parameter in Ref. [43]. Then we study the influence of the SAW strength in section IV B.

##### A. Ideally wetting liquid

We begin our analysis of the influence of the Weber number  $We_s$  by reproducing the case of a completely wetting liquid on a resting horizontal plate without the influence of gravity, which is studied in Ref. [43]. In other words, we consider Eq. (1) with  $Ha = U_0 = \alpha = G = 0$ , fix  $\epsilon_s = 1$  and employ  $We_s$  as control parameter. As explained in the Appendix A [case (ii)], this setting is equivalent to the scaling employed in [43] [and their Eq. (2.23)]. There, steady profiles were obtained using a shooting method, albeit here we employ path continuation.

The resulting bifurcation diagram is presented in Fig. 4 as a black solid line. The blue dashed curve gives the case where the contribution of the hydrostatic gravitational pressure is added ( $G = 10^{-3}$  and  $\alpha = 0$ ). The steady profiles on these branches correspond to a meniscus, which is smoothly and monotonically connected to a homogeneous Landau-Levich film or coating layer. For large  $We_s$ , the film thickness increases monotonically following the power law  $h_c \propto We_s^{2/3}$  identical to the power law dependence on capillary number in the classical Landau-Levich case.

However, the behaviour of the coating system qualitatively changes for smaller  $We_s$ . The dependence of  $h_c$  on  $We_s$  becomes multivalued as each curve features two saddle-node bifurcations. The one occurring at very small  $h_c$  was not detected in Ref. [43]. No film deposition occurs below  $We_s \approx 1.54$  – the threshold value where the crucial saddle-node bifurcation occurs, below which no film deposition occurs; the meniscus profile ends on the truly dry substrate, a situation not

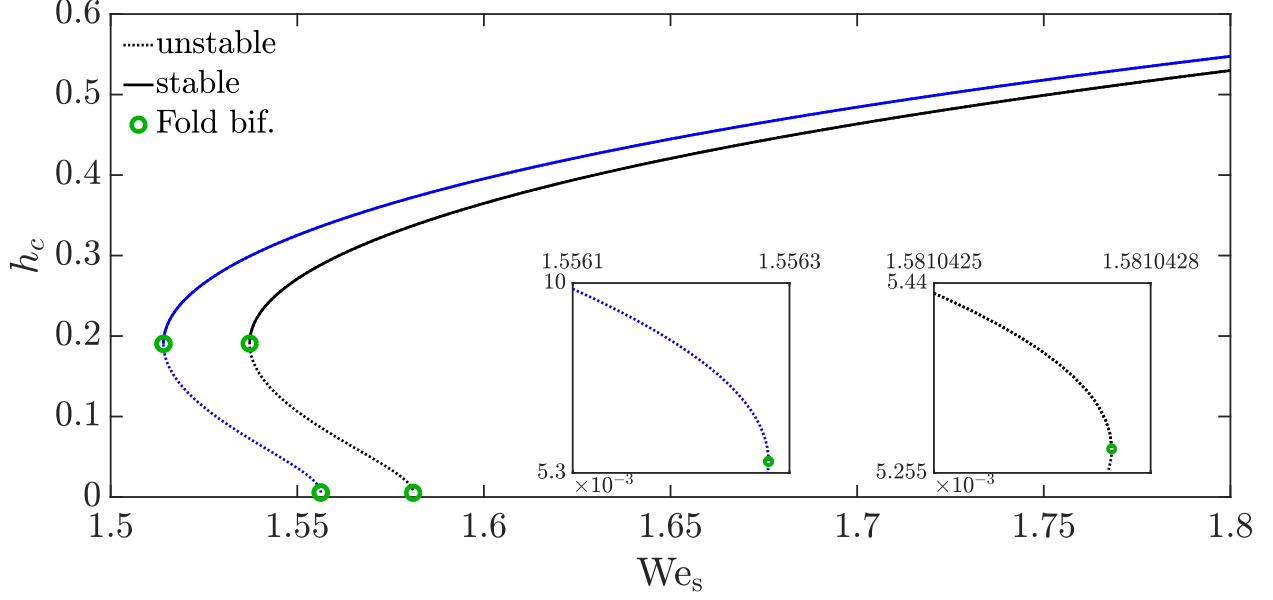


FIG. 4: Bifurcation diagram for a SAW-driven meniscus of a completely wetting liquid ( $Ha = 0$ ) on a resting horizontal plate ( $U_0 = \alpha = 0$ ), which shows the coating film thickness  $h_c$  in dependence of the Weber number  $We_s$  at fixed SAW strength ( $\epsilon_s = 1$ ). The black and blue curve show cases without the contribution of gravity ( $G = 0$ ) as in Ref. [43] and with the contribution of gravity ( $G = 10^{-3}$ ), respectively, while dotted and solid lines represent unstable and stable states, respectively. Saddle-node bifurcations (folds) are marked by green circles. The inset zooms onto the saddle-node bifurcation at very small  $h_c$ . The remaining parameters are  $h_m = 8.1$  and  $L = 40$ .

captured by the model in [43] that does not allow for slip at the contact line.

When following the bifurcation curve from large to small values of  $We_s$ , one firsts observes a gradual decrease in the coating thickness. Then, passing the saddle-node bifurcation at  $We_s \approx 1.54$ , the film deposition state collapses abruptly from the finite thickness  $h_c \approx 0.2$  (cf. Fig. 4). Incorporating gravity, the saddle-node bifurcation is shifted towards smaller values of  $We_s$ , but the corresponding  $h_c$  is nearly constant.

Following the branch through the saddle-node bifurcation, a sub-branch of unstable solutions continues towards larger  $We_s$  values until turning back again (and becoming more unstable) at another saddle-node bifurcation at rather small  $h_c$  values (see insets of Fig. 4). The subsequent tiny sub-branch of unstable states ends when  $h_c$  approaches zero at a critical Weber number. Note that this is not a bifurcation point. Mathematically, the alternative state of a meniscus ending at a true microscopic contact point is a finite support solution. It has a different topology as the Landau-Levich

film solution and can not be obtained with the numerical methods employed here. However, this situation can be amended by explicitly incorporating a description of wettability, as in the following section.

### B. Partially wetting liquid

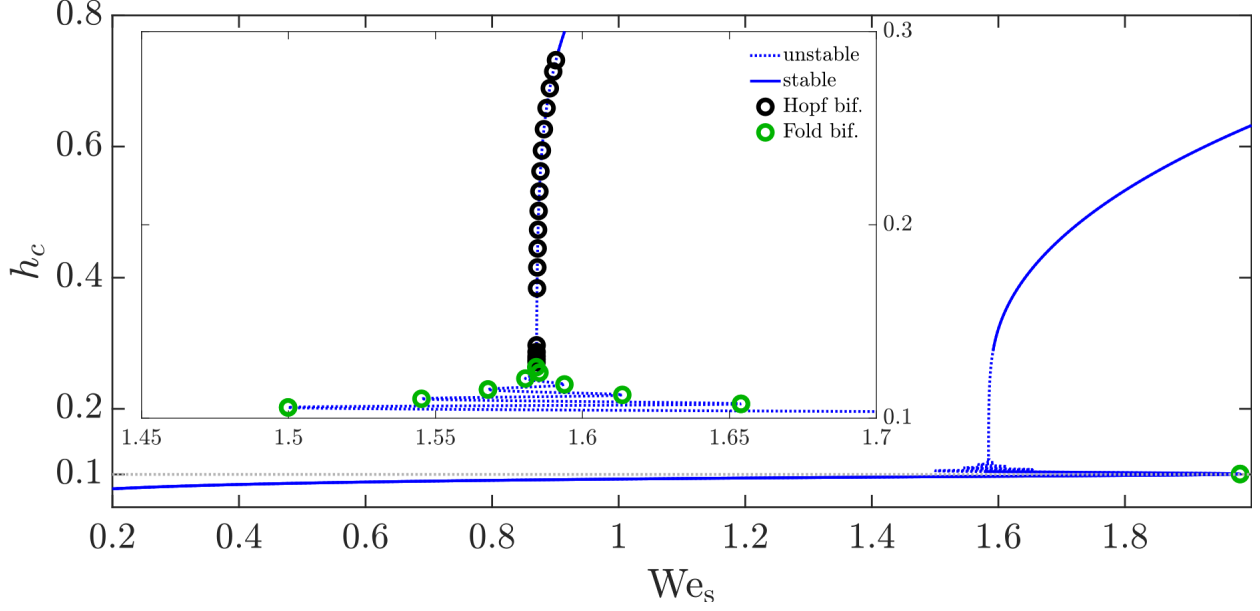


FIG. 5: Bifurcation diagram for a SAW-driven meniscus of partially wetting liquid ( $Ha = 2.0$ ,  $h_p = 0.1$ ) on a resting plate ( $U_0 = 0$ ), which show the coating thickness  $h_c$  in dependence of the Weber number  $We_s$  at fixed SAW strength  $\epsilon_s = 1$ . Dotted and solid lines represent unstable and stable states, respectively. Saddle-node and Hopf bifurcations are marked by green and black circles. The inset zooms onto the region where the curve undergoes “snaking”. The remaining parameters are  $h_m = 8.1$ ,  $G = 10^{-3}$ ,  $\alpha = 0.2$  and  $L = 40$ .

We consider the full evolution equation (1), while accounting for partially wetting liquids (mainly using  $Ha = 2$  and  $h_p = 0.1$ ), but keeping the substrate resting and nearly horizontal ( $U_0 = 0$ ,  $\alpha = 0.2$ ). A truly horizontal substrate gives very similar results but renders details of the continuation procedure more cumbersome. This implies that we still use the scaling of case (ii) in the Appendix A and consider the influence of partial wettability of the results in [43] using  $We_s$  as control parameter. Inspecting the bifurcation diagram in Fig. 5, we notice that the incorporation of partial wettability results in strong changes. For partially wetting liquids described with a wetting

energy, the dry substrate is always covered by a thin adsorption layer of liquid. This implies that the Landau-Levich film state and the finite-support meniscus state, discussed in section IV A, are not topologically different anymore as the former finite-support state becomes a state where the meniscus transitions into the adsorption layer. Therefore, commencing our analysis from large  $We_s$  and then reducing its magnitude, the branch of solutions in Fig. 5 does not end at finite  $We_s$  as in Fig. 4, but continues towards  $We_s = 0$ . We do not show the branch down to  $We_s = 0$  as in this limit the Laplace pressure term diverges what is unphysical. In the following,  $We_s$  is chosen to be sufficiently large so that to avoid this complication, e.g., in Fig. 5 we start at  $We_s \approx 0.3$ . Then, the coating thickness  $h_c$  slowly increases with increasing  $We_s$  until a first saddle-node bifurcation occurs at  $We_s \approx 1.93$ . There,  $h_c$  passes the equilibrium precursor film thickness  $h_p = 0.1$  to increase steadily when following the curve through all bifurcations. Namely, at the first saddle-node bifurcation the curve folds back and stability of states switches from stable to unstable as a first real eigenvalue crosses the imaginary axis. Following the branch  $We_s$  decreases, a second saddle-node bifurcation occurs where an additional real eigenvalue becomes positive as discussed already at Fig. 3 (c) for the case of the classical Landau-Levich coating system. Subsequently, the branch wiggles through another eight saddle-node bifurcations resulting in states that are more and more unstable. This could still be called exponential snaking as the distance between subsequent bifurcations exponentially decreases. However, in contrast to [22] in the case shown here in Fig. 3 (c), the snaking stops after ten saddle-node bifurcations, while in the standard case, the behaviour continues ad infinitum (domain size permitting). In addition, the increasing instability is different from the classical Landau-Levich coating system, where stability changes at each saddle-node bifurcation. However, the finding resembles the behaviour, which is encountered in Langmuir-Blodgett (LB) transfer [29]. Beyond the final saddle-node bifurcation,  $h_c$  increases at nearly constant  $We_s \approx 1.56$ , where the curve slightly bends towards larger  $We_s$  values (see inset of Fig. 5). On this part of the branch eight Hopf bifurcations occur in close succession. Each results in a further coating film destabilization. Following the branch further, we observe another sequence of 13 Hopf bifurcations that successively stabilize the branch, i.e., beyond the final Hopf bifurcation all states are stable. To summarize, the first ten saddle-node bifurcations and eight Hopf bifurcations destabilize the steady states so that 26 eigenvalues cross the imaginary axis; another 13 Hopf bifurcations stabilize the states again. Further increasing  $We_s$ , the branch follows the power law  $h_c \sim We_s^{2/3}$ , which we described before.

We have now analysed how the bifurcation curve changes when switching from an ideally wetting

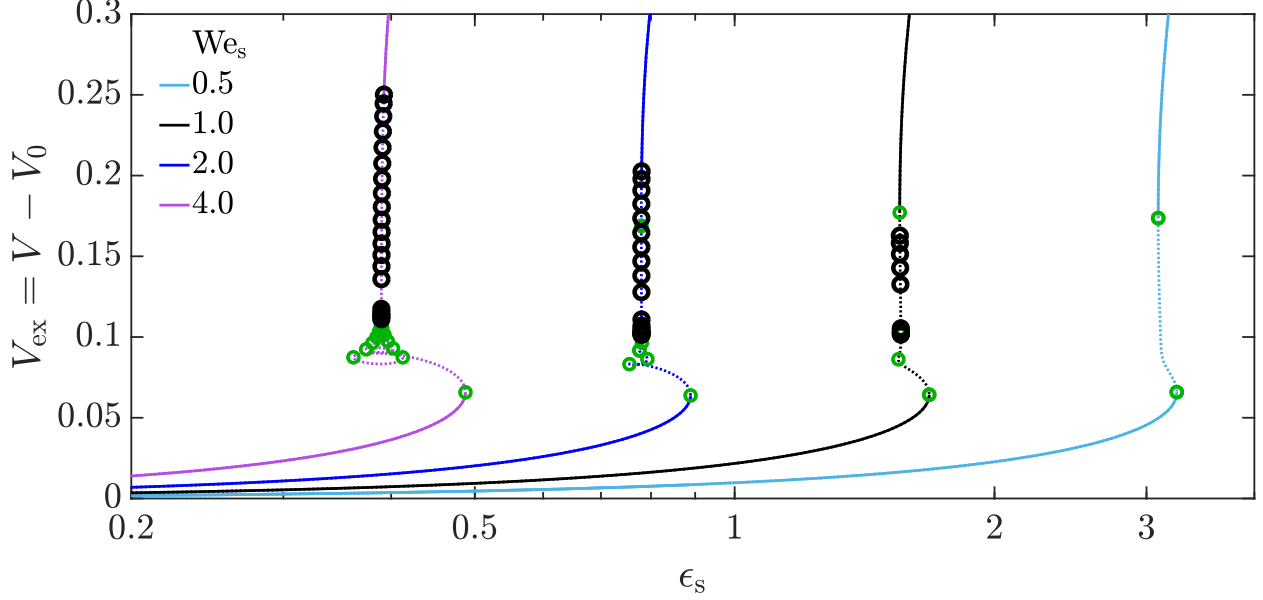


FIG. 6: A bifurcation diagram showing the excess volume  $V_{\text{ex}}$  in dependence of the SAW strength  $\epsilon_s$ , for different Weber numbers  $We_s$  as given in the legend. Further,  $Ha = 1.0$ . Line styles, symbols and remaining parameters are as in Fig. 5. The tracked loci of all bifurcations in the  $(\epsilon_s We_s, \epsilon_s)$ -plane are shown below in Fig. 11.

liquid (studied in section IV A and Ref. [43]) to a partially wetting liquid using  $We_s$  as control parameter. Next, we set  $Ha = 1.0$  thereby switching to the scaling of case (iii) in the Appendix A allowing us to consider the SAW strength  $\epsilon_s$  as control parameter. This enables a more direct comparison to the Landau-Levich system where the plate velocity  $U_0$  is used as control parameter (cf. section III). Corresponding bifurcation diagrams for four different fixed values of  $We_s$  are given in Fig. 6 using again the excess volume  $V_{\text{ex}}$  as solution measure. Overall, all bifurcation curves are similar to the one shown in Fig. 5, but with decreasing  $We_s$  the entire curve shifts towards larger  $\epsilon_s$ . In other words, the system needs more SAW power to spread over the substrate for a smaller ratio of convective stress and capillary stress at the surface. Roughly speaking, at larger  $We_s$  a lower SAW strength is needed to obtain the same excess volume.

We also notice that the number of saddle-node and Hopf bifurcations decreases with decreasing  $We_s$ . All Hopf bifurcations and all but two saddle-node bifurcations have vanished at  $We_s = 0.5$ . This process can be well appreciated when tracking the loci of all bifurcations in the parameter plane spanned by  $We_s$  and  $\epsilon_s$ . Before we discuss this further below, first we discuss the steady thickness profiles and the underlying flow field as characterized by the streamlines. In particular,



we focus on the profiles belonging to the snaking region of the bifurcation curves using the case of  $We_s = 4$  and  $Ha = 1$  in Fig. 6 as an example.

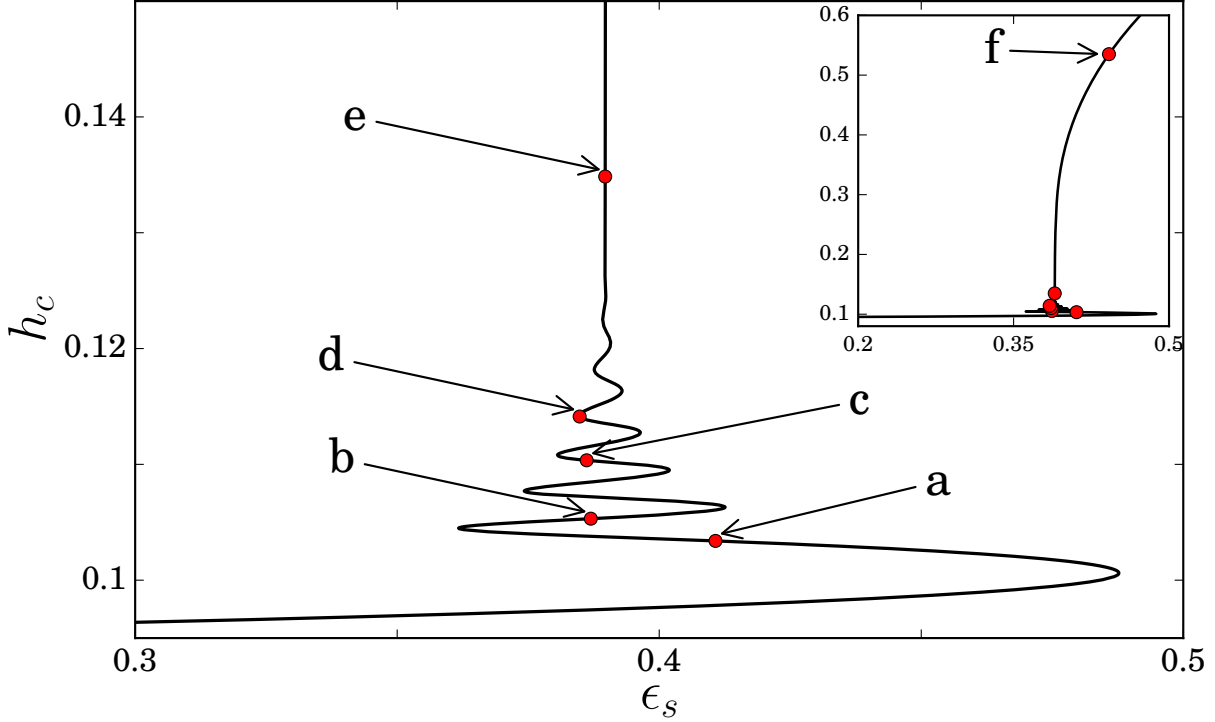


FIG. 7: A magnification of the snaking area of the bifurcation for  $We_s = 4$  and  $Ha = 1$  in Fig. 6, which show the coating thickness  $h_c$  as function of the SAW strength  $\epsilon_s$ . The red filled circles, marked “a” to “f”, indicate loci of steady states, which are presented in Fig. 8.

A corresponding magnification of Fig. 6 is given in Fig. 7. The magnification indicates the loci of the six states presented in Fig. 8. The plots show the steady thickness profiles and the streamlines within the liquid layer. They do not present the complete computational domain but focus on the transition region from the meniscus to the adsorption layer where the foot-like structure develops. Point “a” in Fig. 7 corresponds to the meniscus solution in Fig. 8 (a), i.e., the profile smoothly and monotonically connects the meniscus on the right with the adsorption layer on the left, similar to the black profiles in Figs. 3 (a) to (d). Then, following the snaking curve in Fig. 7 from point “a” to point “d”, a foot-like structure develops and extends. One can see that the SAW induces strong modulations of the foot thickness, which is related to convection rolls within the foot. At the same time, the single large-scale convection roll in the meniscus is nearly unchanged. Following the bifurcation curve further, one observes similar modulations. However, in contrast to the Landau-

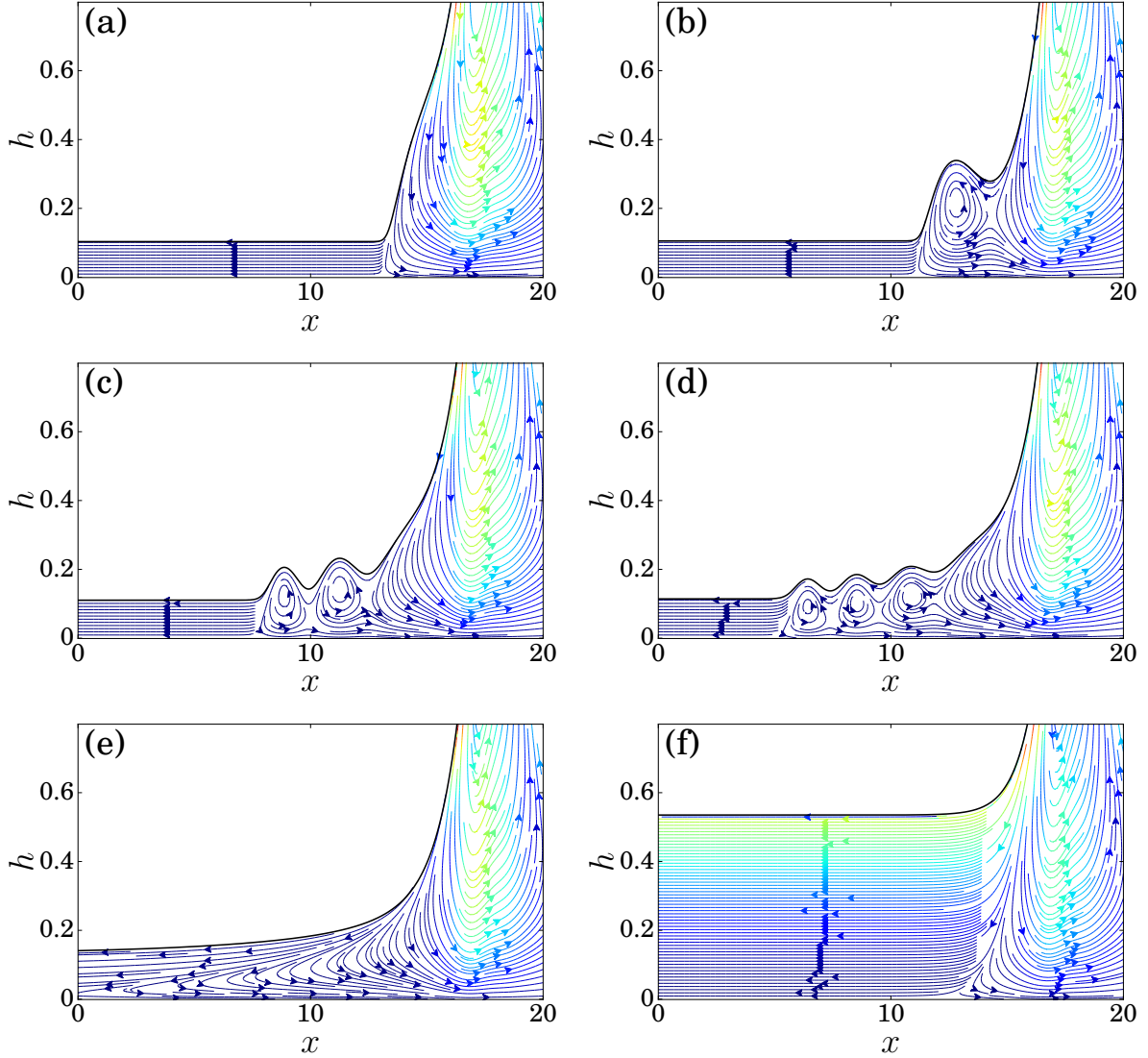


FIG. 8: Panels (a) to (f) show steady film thickness profiles and the corresponding streamlines within the fluid at parameters which are indicated by the letters “a” to “f” in Fig. 7, respectively. In particular, (a) gives a meniscus solution, (b) to (d) present modulated foot solutions, (e) is a transition state between foot and Landau-Levich film state, and (f) gives a Landau-Levich film state.

Levich case in Figs. 3 (a) and (b), the foot does not possess a clearly defined thickness, but becomes thinner with increasing distance from the meniscus. As a result, the transition from the foot to the adsorption layer is continuous. In parallel, the convection rolls in the foot seem to weaken and partially fuse. Profiles right at the end of the snaking region and further along the curve are shown in Figs. 8 (e) and (f). The profiles correspond to standard Landau-Levich films in a similar manner to the red and blue curves in Fig. 3 (c) and (d).

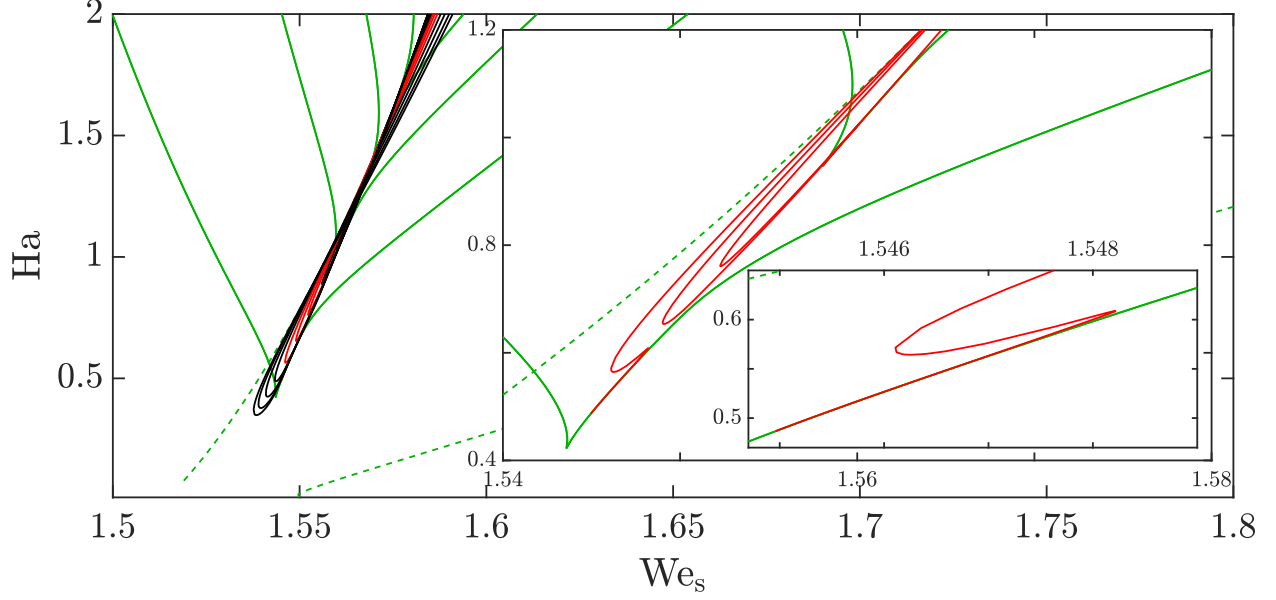


FIG. 9: Shown are the loci of saddle-node (green lines) and Hopf bifurcations (black and red lines) in the parameter plane spanned by the Weber number  $We_s$  and the Hamaker number  $Ha$ . Further line styles are explained in the main text. The insets the region where the leftmost Hopf bifurcation in red emerges from the saddle-node bifurcation, i.e., where a Bogdanov-Takens bifurcation occurs. The remaining parameters are as in Fig. 5.

Up to here, we have investigated individual bifurcation diagrams by employing either the Weber number  $We_s$  or the SAW strength  $\epsilon_s$  as control parameter. In the course of this study, we have detected many saddle-node and Hopf bifurcations. The comparison of their occurrence in dependence on  $\epsilon_s$  for different fixed  $We_s$  has shown that the number of these bifurcations shows stark changes. Our next interest is in the appearance and disappearance of bifurcations in our system. Next we track all bifurcations visible in Figs. 6 and 5 in the  $(\epsilon_s, We_s)$ - and  $(\epsilon_s, Ha)$ -parameter planes.

First, we show in Fig. 9 the loci of saddle-node (green lines) and Hopf bifurcations (black and red lines) in the parameter plane spanned by the Weber number  $We_s$  and the Hamaker number  $Ha$ , i.e., we investigate the interplay of capillarity and wettability. The solid green lines denote saddle-node bifurcations that emerge in pairs in codimension-two hysteresis bifurcations that are cusp-like in the  $(We_s, Ha)$ -plane (see larger-scale inset). In contrast, the two dashed green lines correspond to saddle-node bifurcations that persist in the entire studied parameter range nearly down to  $Ha = 0$ . Note again, that due to numerical issues our computation does not exactly reach  $Ha = 0$ . These

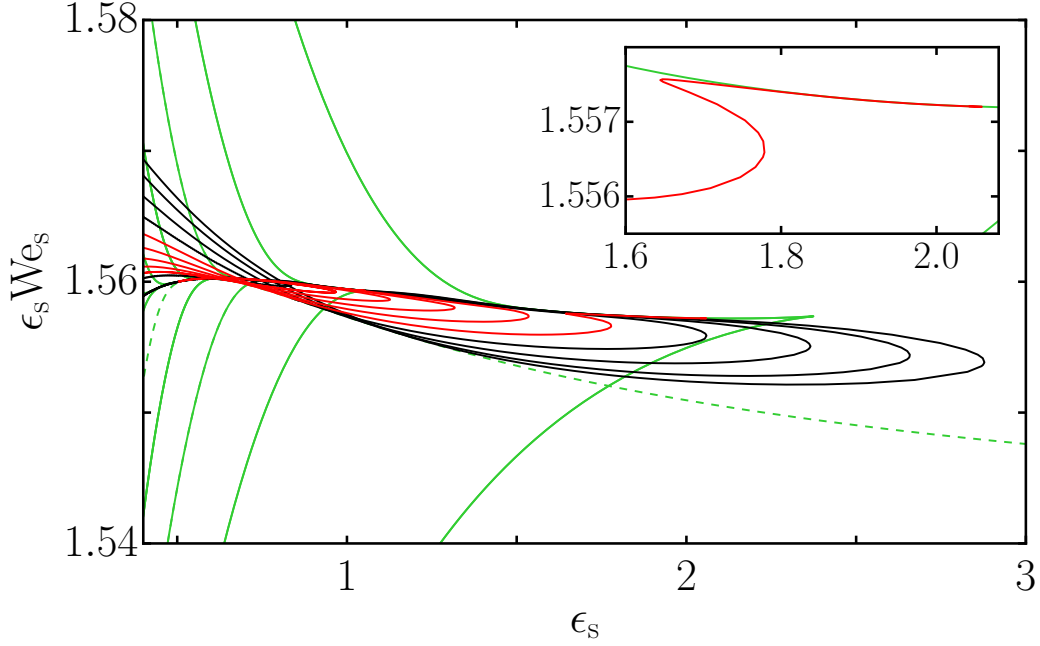


FIG. 10: Loci of saddle-node and Hopf bifurcations are shown in the parameter plane spanned by SAW strength  $\epsilon_s$  and its product with the Weber number  $\epsilon_s We_s$ . The inset magnifies the parameter region where a Bogdanov-Takens bifurcation occurs. Line styles and remaining parameters are as in Fig. 6.

two lines correspond to the saddle-node bifurcations visible in the SAW reference case in Fig. 4. Inspecting the loci of the Hopf bifurcations in Fig. 9, we note that increasing  $We_s$ , the first two Hopf bifurcations appear pairwise in a codimension-two double Hopf bifurcations at  $We_s \approx 1.54$  and  $Ha \approx 0.35$ . The next three pairs appear in the same way. All of them are shown as black lines. However, the next Hopf bifurcation emerges alone from a line of saddle-node bifurcations (see smaller-scale inset of Fig. 9). There, another type of codimension-two bifurcation occurs, namely, a Bogdanov-Takens bifurcation, where the Hopf bifurcation and a global (homoclinic) bifurcation emerge together at a saddle-node bifurcation. Following the corresponding line of Hopf bifurcations, it separates from the line of saddle-node bifurcations and eventually annihilates with another Hopf bifurcation that itself emerged from a fifth double Hopf bifurcation. All further Hopf bifurcations appear in similar ways. Red lines in the figure mark Hopf bifurcations with this type of emergence.

In general, one can say that the number of occurring bifurcations increases with the Weber number (i.e., with decreasing surface tension) and also increases with the Hamaker number  $Ha$  (i.e., with

decreasing wettability). The emergence of Hopf bifurcations is further scrutinized in section IV C.

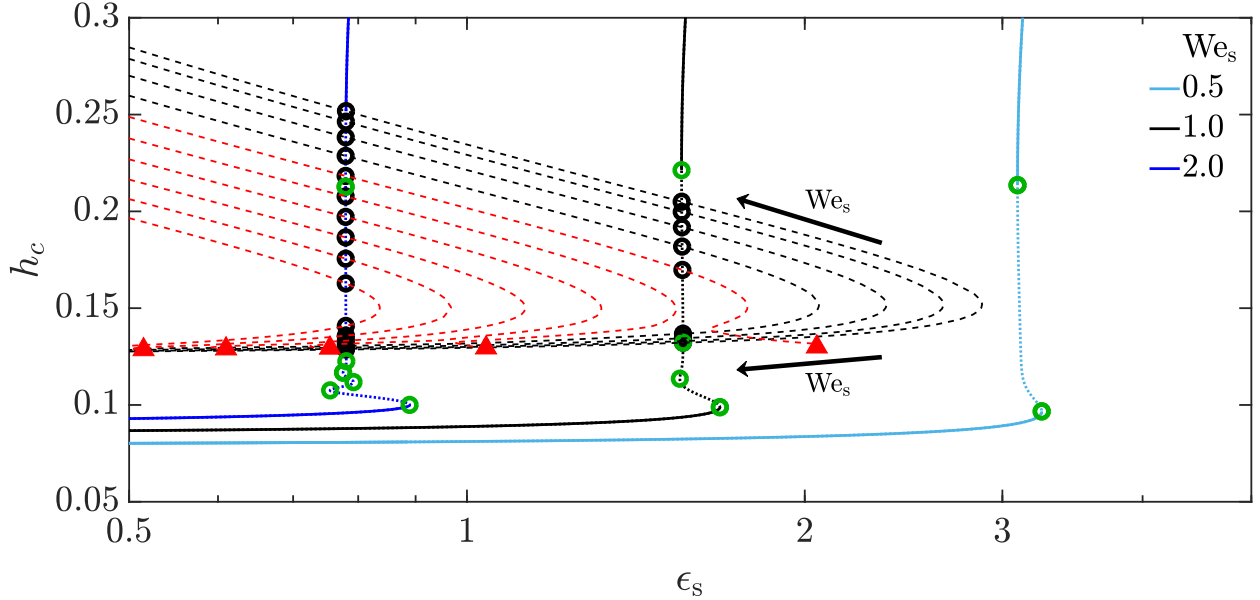


FIG. 11: Bifurcation diagram showing three bifurcation curves from Fig. 6, giving the coating thickness  $h_c$  over SAW strength  $\epsilon_s$  for different  $We_s$ . Additionally, we show as black and red dashed lines how the loci of the Hopf bifurcations change when  $We_s$  is changed. The black arrows indicate the direction of increasing  $We_s$ . The red triangles mark Bogdanov-Takens bifurcations. The remaining parameters are as in Fig. 6.

Next, we track the bifurcations in the  $(We_s, \epsilon_s)$ -plane. An initial inspection of the curves shows that for all tracked bifurcations,  $We_s \sim 1/\epsilon_s$ , and the curves practically coincide in the  $(We_s, \epsilon_s)$ -plane. Therefore, in Fig. 10 we show the curves in the  $(We_s, \epsilon_s We_s)$ -plane where their emergence and relations are well visible.

Furthermore, we illustrate the appearance of the Hopf bifurcations in a different representation by plotting their loci in Fig. 11 as black and red dashed lines together with three bifurcation curves from Fig. 6, that give the coating thickness  $h_c$  over SAW strength  $\epsilon_s$  for different fixed  $We_s$ . The arrows in Fig. 11 indicate the direction of increasing  $We_s$ . The first pair of Hopf bifurcations emerges at  $We_s = 0.52$ .

The colour of the dashed lines indicates, as introduced above, how the Hopf bifurcations appear when  $We_s$  is increased. The black dashed lines represent Hopf bifurcations that emerge through double Hopf bifurcations. The red lines represent Hopf bifurcations that emerge through Bogdanov-Takens bifurcations (marked by red triangles). In particular for the first red line, the above described sequence of events is well visible: first the Hopf bifurcation emerges in the

Bogdanov-Takens bifurcation at  $\epsilon_s \approx 2.06$ , moves towards larger  $We_s$  and smaller  $\epsilon_s$  where it annihilates with a second Hopf bifurcation at  $\epsilon_s \approx 1.78$  that itself appeared in a double Hopf bifurcation at  $\epsilon_s \approx 1.86$ . The latter scheme applies to all Hopf bifurcations beyond the first eight. Overall, this intricate emergence of many Hopf bifurcations results in the creation of many branches of time-periodic states. Each of them connects two bifurcations that are either local or global. In the following, we investigate these branches and their potential reconnections in more detail.

### C. Time-periodic states

In our investigation of the bifurcation behaviour of the 1d SAW system we have encountered a large number of Hopf bifurcations when using the Weber number and SAW strength as main control parameters. Tracking the loci of the bifurcations in parameter planes has indicated that the Hopf bifurcations are created either in double Hopf bifurcations or Bogdanov-Takens bifurcations. Next, we employ PDE2PATH to investigate the branches of time-periodic states (TPS), which emerge at the Hopf bifurcations. Note that recently such branches were described for the dragged-plate system [59] (also compare section III). Here, we provide a deeper analysis by discussing how the single-parameter bifurcation diagram (e.g.,  $\epsilon_s$ ) changes when a second parameter is changed. We are particularly interested in potential reconnections between the different branches of TPS. This is relevant for the present system, but also provides valuable information for the behaviour of the entire class of coating systems.

Before calculating branches of TPI, we begin by discussing the expected behaviour related to the codimension-2 bifurcations where the Hopf bifurcations emerge or vanish. Fig. 12 (a) magnifies the loci of a number of Hopf bifurcations, highlighting in red a line related with particularly intricate behaviour. On the right, panels (b) to (d) sketch qualitatively different bifurcation diagrams (with  $We_s$  as control parameter) with decreasing  $\epsilon_s$ : To the right of the Bogdanov-Takens bifurcation (red triangle), the branch of steady state is 'bare'; bifurcations, which are related to the red branch in (a) do not yet exist (not shown). Then, decreasing  $\epsilon_s$ , when the Bogdanov-Takens bifurcation point marked by a red triangle is passed, a branch of TPS appears which connects a Hopf and a homoclinic bifurcation [Fig. 12 (b)]. Decreasing  $\epsilon_s$  further, another branch of TPS is created in a double Hopf bifurcation at  $\epsilon_s \approx 1.77$  (Fig. 12 (c)). Continuing to decrease  $\epsilon_s$ , Hopf bifurcations, where two different branches of TPS end, approach each other until they annihilate at

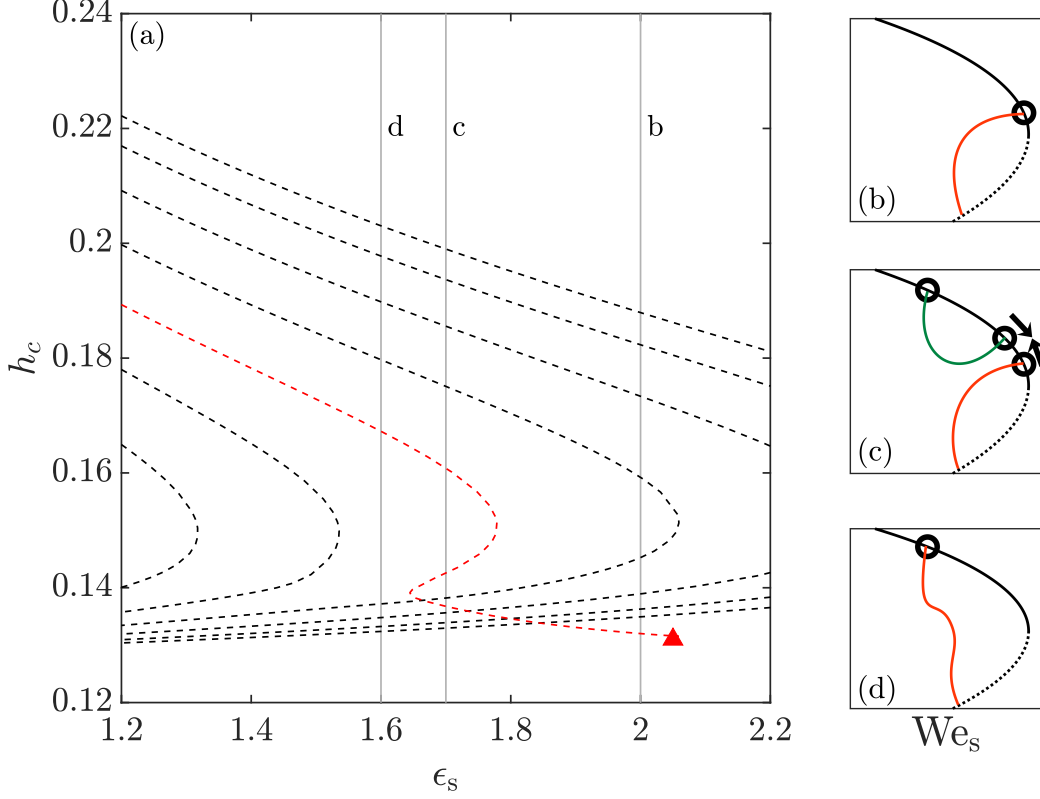


FIG. 12: Panel (a) provides a zoom of Fig. 11 focusing on the loci of a number of Hopf bifurcations, while panels (b) to (d) show sketches of the bifurcation diagrams of time-periodic states (TPS) related to different parameter ranges of the red curve in (a). Typical parameter values where cases (b) to (d) occur are indicated by vertical dotted lines in (a), marked “b”, “c” and “d”. The occurring changes are described in the main text. In (b) to (d), steady states are indicated as solid black lines, while green [red] lines indicate branches of TPS that connect two Hopf bifurcations [a Hopf and a homoclinic bifurcation].

$\epsilon_s \approx 1.65$  in a reverse double Hopf bifurcation effectively, fusing the two branches of TPS into one [Fig. 12 (d)]. Note that the resulting branch may still possess a nontrivial structure, e.g., showing saddle-node bifurcations. These are not tracked here. Note that the remaining branch inherits a Hopf bifurcation and a homoclinic bifurcation as its end points.

To numerically study such qualitative changes we determine bifurcation diagrams, which contain steady states and TPS as a function of SAW strength  $\epsilon_s$  for an increasing sequence of fixed Weber numbers,  $We_s$ . We commence our analysis in Fig. 13 (a) and (b) with two relatively simple diagrams at fixed  $We_s = 0.55$  and  $We_s = 0.72$ , respectively. We observe two and six Hopf bifurcations, respectively, and no global bifurcations. Increasing  $We_s$ , we observe at  $We_s = 0.8$  an odd number of nine Hopf bifurcations, see Fig. 14. This implies that a first Bogdanov-Takens

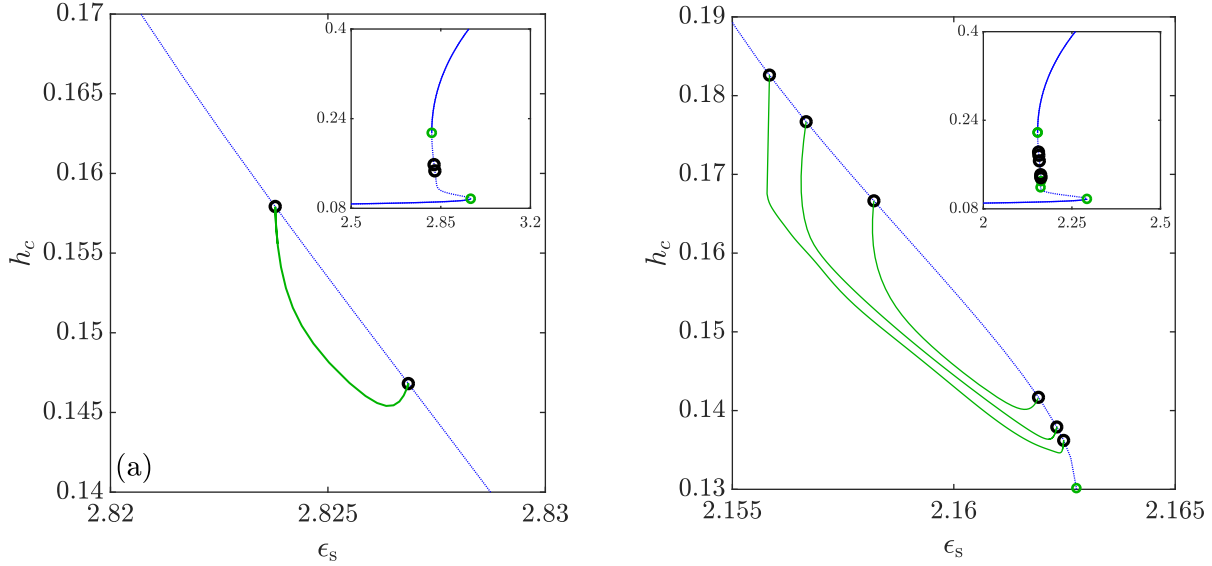


FIG. 13: Panels (a) and (b) give selected parts of the bifurcation diagrams, which show the (time-averaged) coating film thickness  $h_c$  as a function of the SAW strength  $\epsilon_s$  at the fixed Weber number values  $We_s = 0.55$  and  $We_s = 0.72$ , respectively. Blue and green lines represent steady and time-periodic states, respectively. Hopf bifurcations are marked by black circles. The remaining parameters are as in Fig. 11. The insets give the relevant complete bifurcation curve for the steady states.

bifurcation must have occurred and that the additional appearance of a homoclinic bifurcation is expected.

In Fig. 14 we present a bifurcation diagram for  $We_s = 0.8$  that shows nine Hopf bifurcations on the branch of steady states. In the snaking region, a very short part of the branch shows linearly stable solutions, namely the part between the Hopf bifurcation and the saddle-node bifurcation in Fig. 14 (b). The related branch of TPS seems unusual as it starts and ends on the same side of the saddle-node bifurcation, in contrast, to the normal behaviour expected of such a branch, which is created in a Bogdanov-Takens bifurcation [32]. Since the branch has indeed emerged at this saddle-node bifurcation, it is likely that further codimension-2 events have taken place at this saddle-node bifurcation, e.g., a fold-Hopf bifurcation. The point could be further investigated in the future. The overall scenario indicates that the branch of TPS is linearly stable when it emerges supercritically at the Hopf point. This is consistent with the changes in stability observed when following the branch of steady states with increasing  $\epsilon_s$  from small values: One starts with a stable meniscus state, passes first two destabilizing saddle-node bifurcations (inset of Fig. 14 (a)), then a global bifurcation (not affecting stability) and finally the discussed Hopf bifurcation where both unstable eigenmodes stabilize. The third saddle-node bifurcation, zoomed onto in Fig. 14 (b) (at



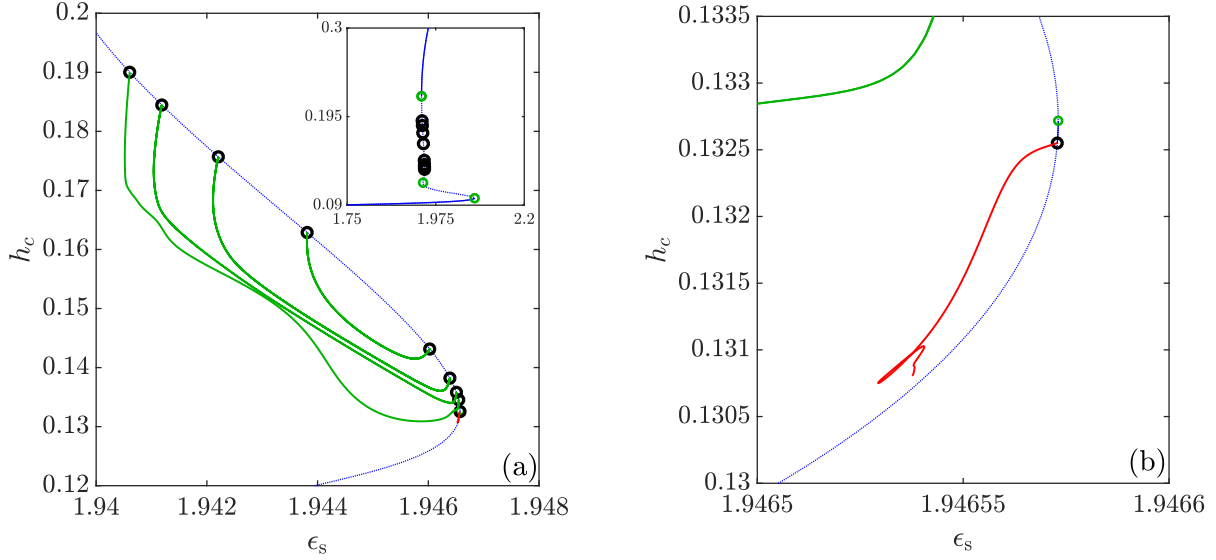


FIG. 14: Panel (a) gives a bifurcation diagram showing the (time-averaged) coating thickness  $h_c$  as a function of the SAW strength  $\epsilon_s$  at fixed Weber number  $We_s = 0.8$ . Remaining parameters, line styles, symbols and inset are as in Fig. 13. The branches of TPS, which connect two Hopf bifurcations are shown in green, while the single branch connecting a Hopf and a homoclinic bifurcation is shown in red. As in (a) it is nearly not visible, panel (b) gives a zoom of the region very close to the saddle-node bifurcation of the steady states. The corresponding dependencies of the period of the TPS on  $\epsilon_s$  is presented in Fig. 15.

$h_c \approx 0.1328$ ) destabilizes the steady state again.

Note that the branch of TPS presents a particular numerical challenge when approaching the global bifurcation since the period  $T$  is expected to diverge. With the employed numerical method we are not able to approach the bifurcation closely. However, Fig. 15 supports our interpretation. Its two panels show the period  $T$  as a function of the SAW strength  $\epsilon_s$  for all branches of TPS in Fig. 14. One finds in panel (a) that  $T$  for the branch related to the global bifurcation (red line), is much larger than  $T$  for the branches, which connect two Hopf bifurcations (green branches zoomed onto in panel (b)). Further,  $T$  steeply increases for the red branch indicating the likely divergence when approaching the global bifurcation.

Next, we further increase the Weber number to  $We_s = 0.9$  and show the resulting bifurcation diagram in Fig. 16. There are now six branches of TPS, which connect eleven Hopf bifurcations. The corresponding periods are given in Fig. 17, indicating a strong increase in the period of the branch that approaches the global bifurcation. Although, overall the picture is similar, there are a number of important changes. In Fig. 14 at  $We_s = 0.8$  the global bifurcation had just appeared and connected to a Hopf bifurcation nearby (all in the vicinity of the saddle-node bifurcation of steady

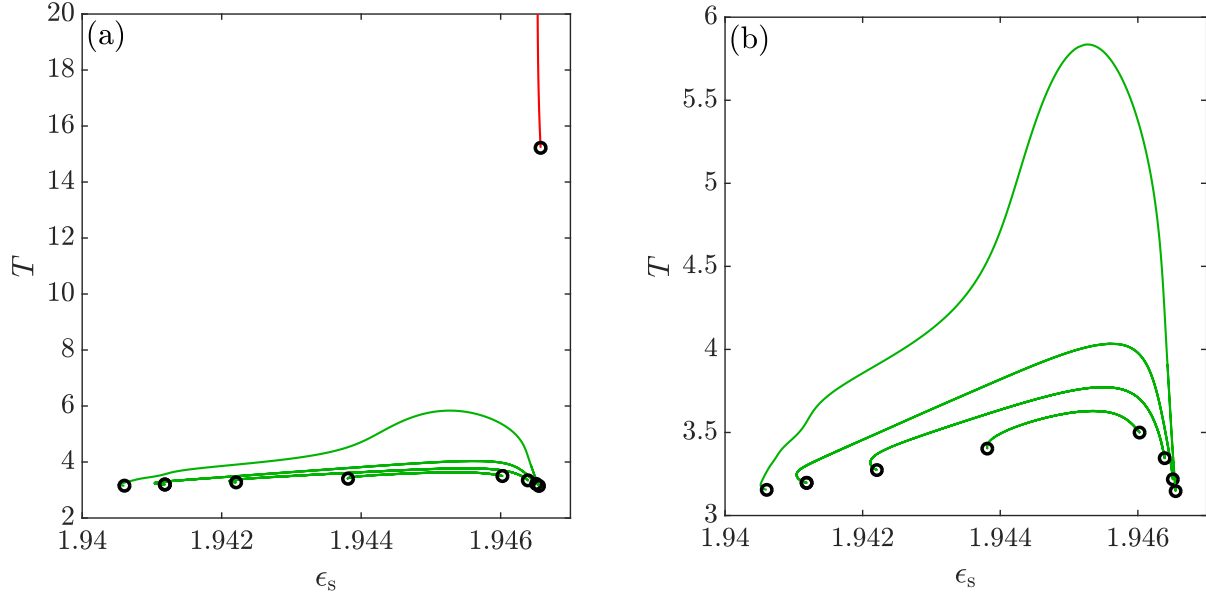


FIG. 15: Time period  $T$  as function of the SAW strength  $\epsilon_s$  for all branches of TPS in Fig. 14. Line styles are as in Fig. 14. Panel (b) zooms onto the four branches that connect two Hopf bifurcations.

states). Now, at  $We_s = 0.9$ , the global bifurcation connects to the Hopf bifurcation at smallest  $\epsilon_s$ , i.e., either many reconnections have taken place or the relevant Hopf bifurcation has passed all other Hopf bifurcations. Inspecting the transition between  $We_s = 0.8$  and  $We_s = 0.9$  in detail we find that there is a combination of moving bifurcations and reconnections of branches of TPS when changing the magnitude of  $We_s$  from 0.8 to 0.9.

For clarity we illustrate the complicated sequence of events in the schematic provided in Fig. 18. Panel (a) shows all Hopf bifurcations at  $We_s = 0.8$  as they occur along the branch of steady states together with their connections. That is, the topology of Fig. 18 (a) is identical to Fig. 14: four directly connected pairs of Hopf bifurcations (green) and one Hopf bifurcation connected to a global bifurcation (red). This state defines the numbering of the bifurcations in Fig. 18: the pairs “1-1\*” to “4-4\*” and the individual pair “A-g”, where “g” stands for the global bifurcation.

The first topological change occurs when the A-g branch approaches the 1-1\* branch. First, the bifurcation A passes bifurcation 1, and slightly afterwards the branches reconnect such that afterwards branches 1-A and 1\*-g exist, see Fig. 18 (b), i.e., Hopf bifurcation 1\* is now connected to the global bifurcation. This corresponds to the state in Fig. 16.

As bifurcation A moves further to the right, it swaps position with bifurcation 2 [Fig. 18 (c)]. Then, a bit later another reconnection is triggered and as a result branches 1-A and 2-2\* become branches 1-2\* and 2-A of Fig. 18 (d). Subsequently, more reconnections occur as bifurcation A

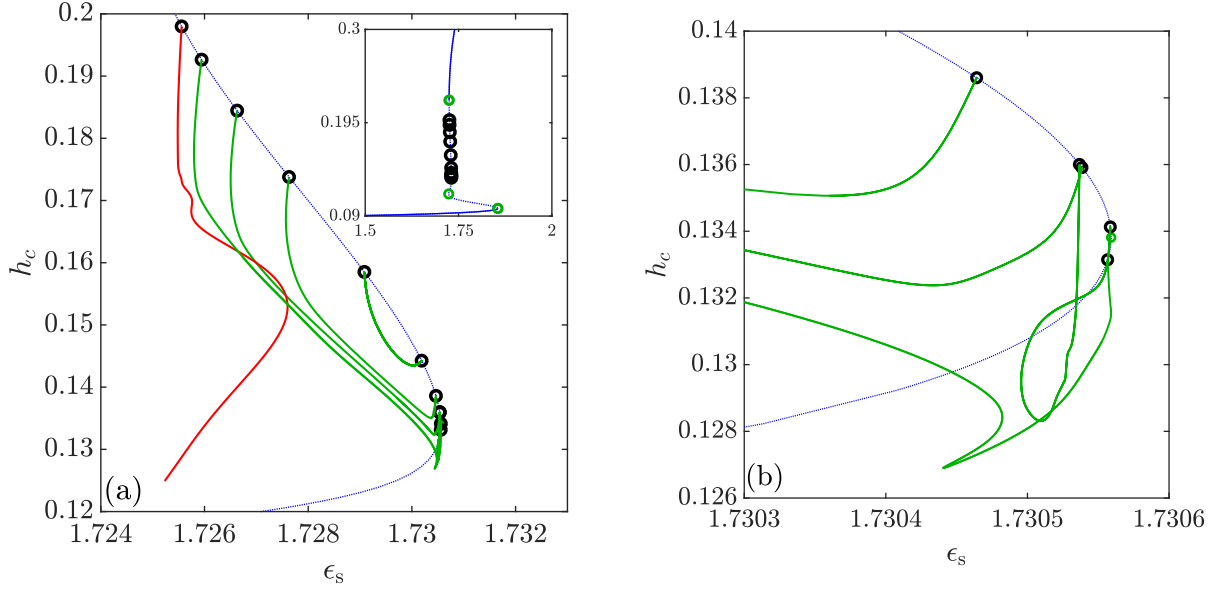


FIG. 16: Panel (a) gives a bifurcation diagram showing the (time-averaged) coating thickness  $h_c$  in dependence of the SAW strength  $\epsilon_s$  at fixed Weber number  $We_s = 0.9$ . Remaining parameters, line styles, symbols and inset as in Fig. 14. Panel (b) gives a zoom of the region very close to the saddle-node bifurcation of the steady states. The corresponding dependencies of the period of the TPS on  $\epsilon_s$  is presented in Fig. 17.

continues moving to the right [Figs. 18 (d) to (f)]. The picture becomes slightly more involved when between panel (d) and (e) another branch 5-5\* appears and gets involved in the reconnection game. Roughly speaking, the appearance corresponds to the leftmost fold on the red dashed curve in Fig. 12. The final step, from Fig. 18 (g) to (h) occurs when branches 4-A and 5-5\* reconnect into one branch A-5\*, thereby eliminating Hopf bifurcations A and 5. This corresponds to the leftmost fold on the red dashed curve in Fig. 12.

The final state Fig. 18 (h) has an appearance very similar to the first one (a), only the connection to the global bifurcation has moved from the leftmost bifurcation to the rightmost one. Properly calculating the diagrams, the final state of the described sequence is obtained for  $We_s = 1.0$  [see Fig. 19]. Note that there is a slight mismatch between sketch and bifurcation diagrams as the sketch focuses on the reconnections, but ignores the additional branch appearing in a double Hopf bifurcation between Figs. 14 and 16.

Overall, in this cascade of topological changes of the bifurcation diagram, all branches of TPS are reconnected once, so that finally each surviving Hopf bifurcation  $n$  (that was initially connected to Hopf bifurcation  $(n)^*$ ) is connected to bifurcation  $(n+1)^*$ . The entire described sequence of events

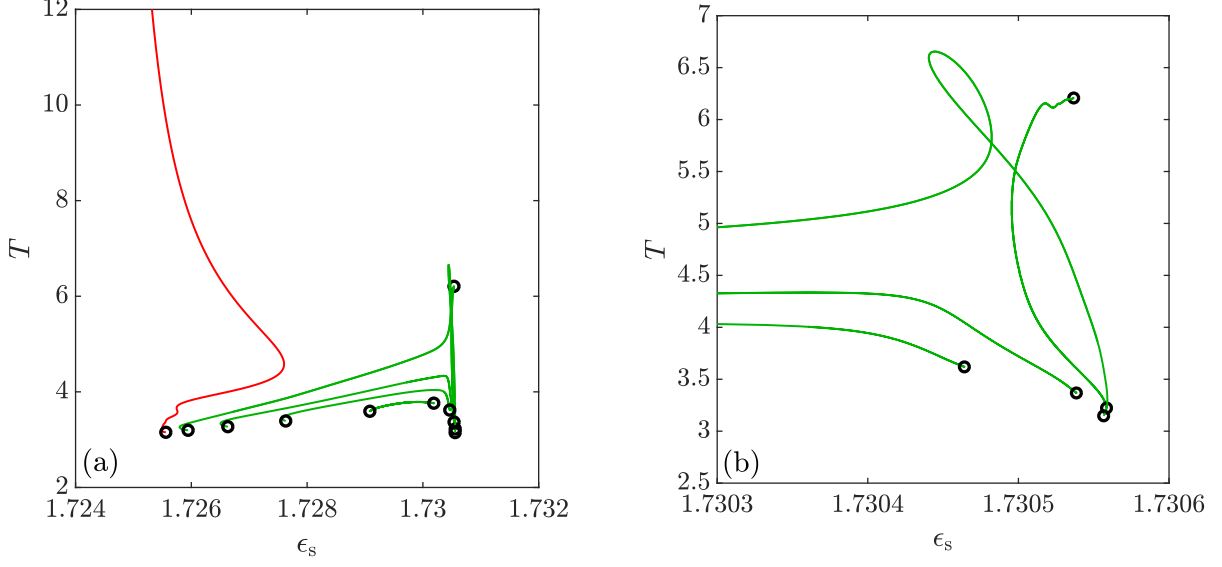


FIG. 17: Time period  $T$  is shown as a function of the SAW strength  $\epsilon_s$  for all branches of TPS in Fig. 16, line styles are identical. Panel (b) provides a zoom.

is triggered each time a Bogdanov-Takens bifurcation occurs. Hence, the overall rearrangement of the bifurcation diagram involves a large number of codimension-2 events.

We exemplify this, by presenting in Fig. 20 a bifurcation diagram at larger  $We_s = 2.0$ . The corresponding dependence of the period  $T$  on  $\epsilon_s$  is shown in Fig. 20. There exist 11 branches of TPS. Four connect Hopf and homoclinic bifurcations, the other seven pairs of Hopf bifurcations. Of the four branches involving a global bifurcation, three have already terminated the sequence of reconections described above, however, the fourth one still has to undergo the sequence. Inspecting the individual branches we see that they acquired a more complex structure and now feature many more saddle-node bifurcations. This tendency is stronger for the outer branches than for the inner one. Also the range of periods increases for the branches connecting two Hopf bifurcations.

Finally, we briefly discuss the characteristics of the time-periodic states. Panels (c) to (f) of Fig. 20 show four space-time plots of selected TPS at loci indicated in panel (a), all on the same branch of TPS, namely, the “outermost” branch, i.e., the branch that emerges first when decreasing  $\epsilon_s$ . In all cases, drops are shed from the foot structure and then move at about constant speed along the substrate until they leave the domain. Close to this point they get slightly deformed due to boundary effects that, however, do not influence the main part of their trajectory. Moving along the branch of TPS away from the Hopf bifurcation, where it emerges, the number of drops in the domain becomes smaller as the shedding events that define the period  $T$  become less frequent. The foot structure where the drops emerge does not change very much along the branch. This,

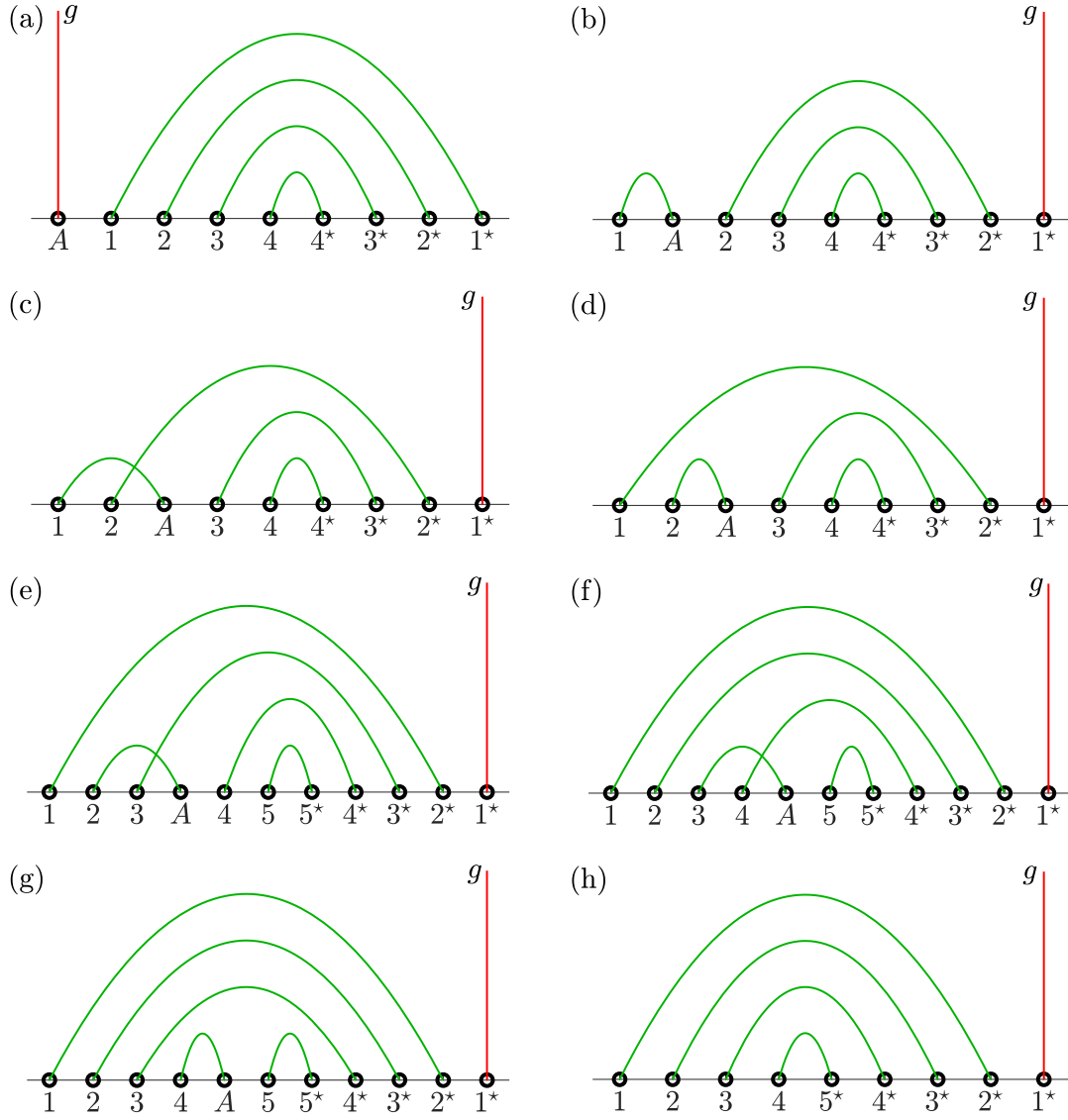


FIG. 18: Illustration of the motion of Hopf bifurcations and the related reconnections of the branches of TPS. The different steps are schematically represented in parts (a) to (h) with line styles as in Fig. 15. The vertical axes symbolically represents a solution measure, e.g., period  $T$ . Vertical lines indicate connection to a homoclinic bifurcation.

however, is in marked contrast when inspecting the TPS on other branches (not shown). The difference between the various branches mainly lies in the details of the foot structure like its length and the number of visible undulations.

With this we end our investigation of the various branches of time-periodic states that has shown the richness of the solution structure of the SAW driven system.

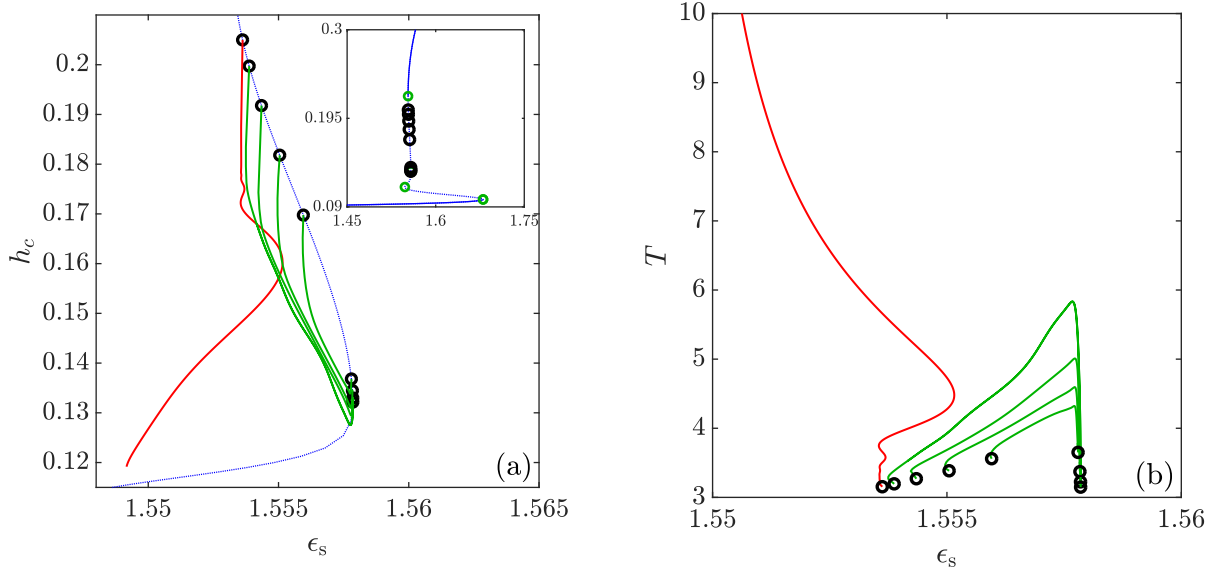


FIG. 19: (a) Bifurcation diagram showing the (time-averaged) coating thickness  $h_c$  in dependence of the SAW strength  $\epsilon_s$  at fixed Weber number  $We_s = 1.0$ . Remaining parameters, line styles, symbols and inset as in Fig. 14. Panel (b) gives the corresponding dependencies of the period of the TPS on  $\epsilon_s$ .

## V. CONCLUSION

In the present work we have in some detail studied the bifurcation structure corresponding to a liquid meniscus driven by surface acoustic waves (SAW). In particular, we have combined a precursor-based thin-film model for the classical Landau-Levich (or dragged plate) problem for partially wetting liquids studied earlier in Refs. [22, 59, 67] with the thin-film model for the SAW-driven meniscus considered in Ref. [43]. This has enabled us to investigate the two systems in a common framework, first to reproduce selected results for each of them, and then to look at the behavior of the SAW-driven system in the case of partially wetting liquids in direct comparison to results obtained for the Landau-Levich system. Our investigation has been based on numerical path continuation techniques.

We have focused on one-dimensional substrates, i.e., we have neglected transversal perturbations, and have investigated in detail how the various occurring steady and time-periodic states depend on the Weber number and the SAW strength. The full bifurcation structure related to qualitative transitions caused by the SAW has been uncovered with a particular attention on Hopf bifurcations related to the emergence of time-periodic states. The latter correspond to the regular shedding of lines from the meniscus. The interplay of several of these bifurcations has been investigated by tracking the bifurcations in selected parameter planes, thereby discussing the codimension-

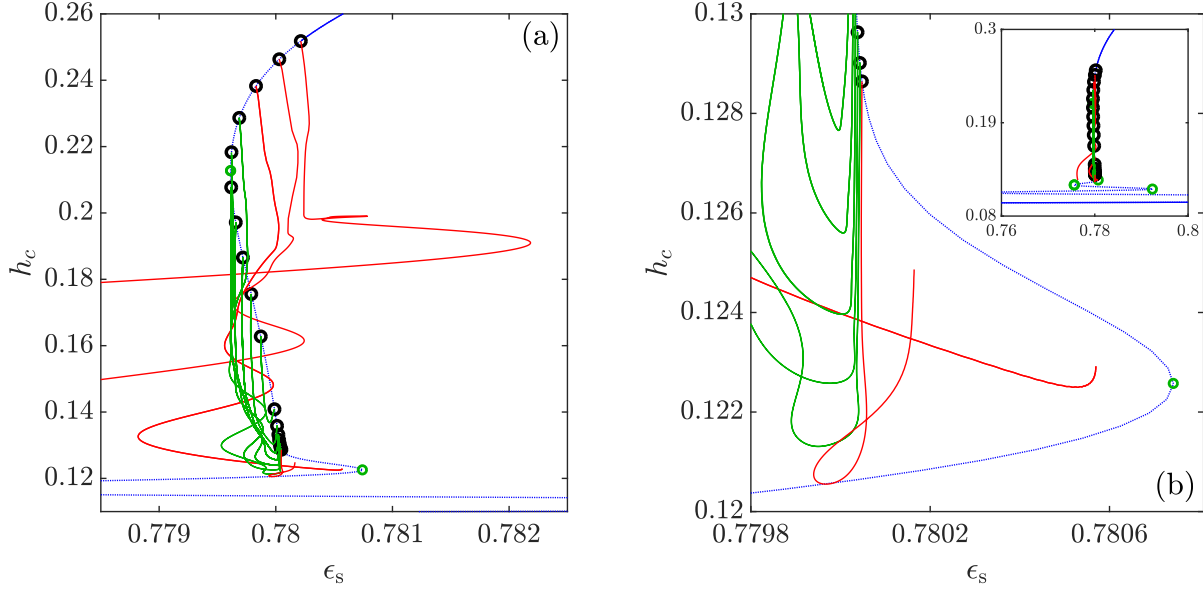


FIG. 20: Bifurcation diagram, which shows the (time-averaged) coating film thickness  $h_c$  as function of the SAW strength  $\epsilon_s$  at the fixed Weber number  $We_s = 2.0$ . The full diagram is shown as inset in panel (b) and panels (a) and (b) magnify the most interesting regions. Remaining parameters, line styles, and symbols are as in Fig. 14. Fig. 21 shows the corresponding dependencies of the period of the TPS on  $\epsilon_s$  and selected spacetime plots of TPS.

2 bifurcations where they emerge and disappear. In this way, our study has provided detailed information relevant to the entire class of dragged-film and forced-meniscus problems. It well aligns with and extends results on the bifurcation structure obtained for the mentioned Landau-Levich problem for partially wetting liquids as well as for line deposition in Langmuir-Blodgett transfer [29, 30].

Compared to the Landau-Levich problem for partially wetting liquid [22], in the SAW-driven case, we have identified the same type of basic solutions, namely, a meniscus state, where a contact line region separates a meniscus and a precursor film, a foot state, where a foot-like structure protrudes from the meniscus and a Landau-Levich film state where a relatively thick homogeneous film is coating the substrate. Its thickness follows a similar power law as in the classical Landau-Levich system.

However, in contrast to the Landau-Levich problem, in the SAW-driven case the foot states show rather strong thickness modulations along the foot and a more continuous transition towards the precursor layer at the tip of the foot. Note that such modulations can exist in the dragged-plate case, but are much weaker and about a well defined foot thickness [67]. The individual transitions

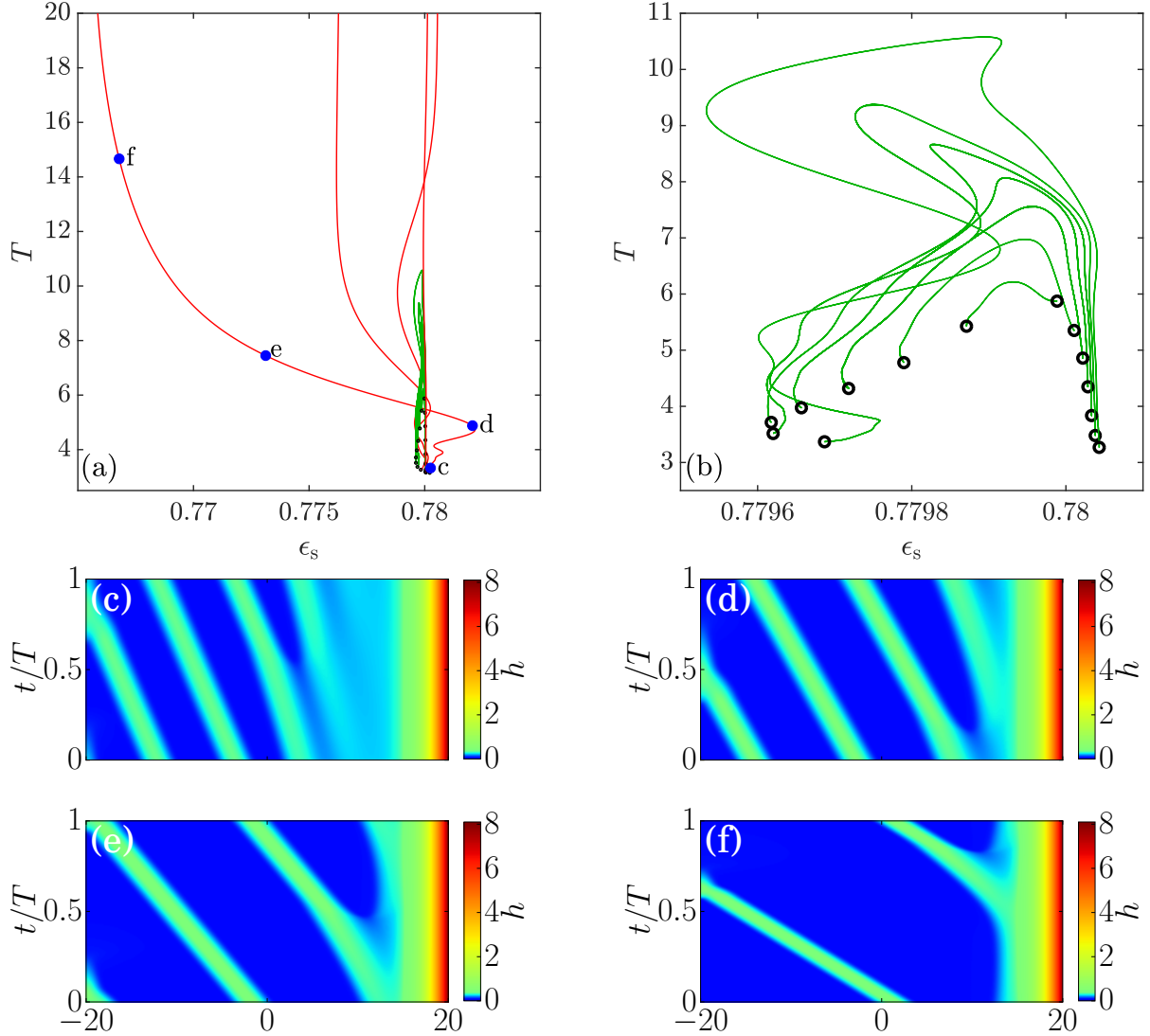


FIG. 21: Time-period  $T$  is shown as a function of the SAW strength  $\epsilon_s$  for all branches of TPS in Fig. 20, line styles are identical. Panel (b) provides a zoom while panels (c) to (f) show space-time plots of selected TPS at loci indicated in panel (a) by corresponding labels “c” to “f”, where (c)  $T = 3.72$ , (d)  $T = 4.88$ , (e)  $T = 7.45$  and (f)  $T = 14.66$ .

between the three types of steady states have been found to be similar when changing the main control parameters Weber number and SAW strength. However, the transitions differ when comparing them to the dragged-plate system. Here, the foot states are situated on a snaking part of the bifurcation curve. Virtually, all of them are unstable, while in the dragged case they consecutively switch between stable and unstable. The continuous transition between the snaking part of the bifurcation curve and the part on the same curve that corresponds to Landau-Levich films is a



feature of the SAW-driven case that has not been observed in the dragged-plate case. There, the snaking curves always diverge at finite driving accompanied by a diverging foot length. This is not the case here.

Overall, the bifurcation structure has turned out to be rather involved, the general tendency being that its complexity increases with increasing Weber number and also with decreasing wettability. More and more saddle-node and Hopf bifurcations appear together with the branches of time-periodic states emerging from the latter. Such branches are also observed for the dragged-plate system [59], but have here been investigated in more depth. In particular, we have shown how these branches appear through double Hopf bifurcations and Bogdanov-Takens bifurcations that also create global bifurcations. We expect this to be similar in the dragged-plate case and related coating systems. On a qualitative level, our corresponding results are similar to the ones for Langmuir-Blodgett transfer [30] further strengthening the point, put forward, e.g., in [62, 72] that these systems share many features and that the investigation of generic models as in [24] is rather important.

Our results show that a very finely tuned SAW-driven system could possibly be switched between the deposition of a homogeneous film and the deposition of line or droplet patterns and control by SAW could be used together with other means of control as the usage of prestructured plates [73, 74] or variable plate dragging speed [38]. To study the application of SAW control to deposition from solutions or suspensions with volatile solvent [42], solute dynamics and solvent evaporation have to be incorporated into the model by amending corresponding models reviewed in [15, 62, 63].

However, our results also indicate that the parameter region where all these changes occur is very small and might be difficult to access with the present experimental techniques. Therefore, our results should not be taken as predictive in a quantitative way but as a catalogue of qualitative transitions expected in a variety of coating systems. As discussed in the conclusion of Ref. [59], there exists a number of experimental systems that show related qualitative transitions. These include (i) water drops sliding on an oil film which can be destabilized by an applied voltage and transform into many small oil droplets underneath the water drop [57] (also see [7]); (ii) recent experiments on gas bubbles that move through a tube filled with partially wetting liquid where the liquid film between bubble and wall may undergo related instabilities [31], and (iii) the different dynamic regimes of relatively thick viscous liquid films flowing down a cylindrical fiber [26]. For the detailed discussion of these experiments in the context of time-periodic states in the dragged-

plate case see the conclusion of Ref. [59]. In all these systems, SAW may be employed to stabilize the Landau-Levich(-Bretherton) films.

Finally, we stress again that our investigation has been entirely focused on one-dimensional systems. However, driven contact lines and deposition dynamics often shows transversal instabilities [62]. This have been excluded from our study. A first investigation [37] has shown, that there exist bifurcations that break the transversal invariance and result in branches of fully two-dimensional states that represent a rich set of structures. However, a systematic study of their properties is a formidable future endeavor that should also aim at an understanding of time-periodic two-dimensional states occurring in various coating systems.

### Acknowledgement

We acknowledge support by the German-Israeli Foundation for Scientific Research and Development (GIF, Grant No. I-1361-401.10/2016), as well as further support by the Deutsche Forschungsgemeinschaft (DFG; Grant No. TH781/8-1). We also thank Sebastian Engelnkemper for the creation of a first tutorial on PDE2PATH usage for dragged-film problems, as well as Tobias Frohoff-Hülsmann and Simon Hartmann for support with PDE2PATH and OOMPH-LIB implementations, respectively.

### Appendix A: Nondimensionalization

The appendix discusses our scaling and relates it to the scalings employed in Refs. [43] and [22], respectively. The dimensionless thin-film equation given by Eq. (2.23) of Ref. [43] writes

$$\partial_t h = -\partial_x \left[ \frac{h^3}{3\text{We}_s} \partial_{xxx} h + h v_s(h) \right]. \quad (\text{A1})$$

Re-introducing their scales

$$\tau = \frac{L}{\chi U \text{Re}}, \quad \delta, \quad \text{and} \quad L = \frac{\delta}{\epsilon}, \quad (\text{A2})$$

for time  $t$ , film thickness  $h$ , and  $x$ -coordinate, respectively, and using the dimensionless numbers

$$\text{We}_s = \frac{\chi \text{ReCa}}{\epsilon^3} \quad \text{and} \quad \text{Ca} = \frac{\mu U}{\gamma}, \quad (\text{A3})$$

we obtain the dimensional evolution equation

$$\partial_t h = -\partial_x \left[ \frac{h^3}{3\mu} \gamma \partial_{xxx} h + U_w h v_s(h) \right] \quad (\text{A4})$$

where now  $x$ ,  $t$ , and  $h$  are dimensional and  $U_w = \rho\chi\delta U^2/\mu$  is a typical velocity.

The complete dimensional thin-film evolution equation that governs the standard Landau-Levich problem for a partially wetting liquid with additional SAW-driving and a dragged plate is given by

$$\partial_t h = -\partial_x \left\{ \frac{h^3}{3\mu} [\partial_x (\gamma \partial_{xx} h + \kappa \Pi(h) - \rho g h) + \alpha \rho g] + U_w h v_s(h) + u h \right\} \quad (\text{A5})$$

where  $\Pi(h)$  is a dimensionless Derjaguin pressure and  $\kappa$  the related energy density scale. The parameter  $\alpha$  is the physical inclination angle and  $u$  is the velocity of the moving plate.

Now we introduce the scales

$$\tau = \frac{L}{\nu}, \quad \delta, \quad \text{and} \quad L = \frac{\delta}{\epsilon} \quad (\text{A6})$$

for time, film thickness, and  $x$ -coordinate, respectively. Here  $\nu$  is a generic velocity scale, that will be specified later when deriving the different scalings used here and in the literature. We obtain the nondimensional equation

$$\partial_t h = -\partial_x \left\{ \frac{h^3}{3} \partial_x (D_1 \partial_{xx} h + D_2 \Pi(h)) + D_3 \frac{h^3}{3} \left( \frac{\alpha}{\epsilon} - \partial_x h \right) + D_4 h v_s(h) + D_5 h \right\} \quad (\text{A7})$$

with the nondimensional numbers

$$D_1 = \frac{\epsilon^3 \gamma}{\mu \nu}, \quad D_2 = \frac{\epsilon \kappa \delta}{\mu \nu}, \quad D_3 = \frac{\epsilon \rho g \delta^2}{\mu \nu}, \quad D_4 = \frac{U_w}{\nu}, \quad D_5 = \frac{u}{\nu}. \quad (\text{A8})$$

$D_1$  is an inverse Capillary or Weber number,  $D_2$  may be called a Hamaker number,  $D_3$  is a Gravity or Galileo number,  $D_4$  a velocity ratio corresponding to a SAW strength, and  $D_5$  a velocity ratio corresponding to a plate dragging strength. Keeping  $\nu$  general, i.e., not selecting any leading balance, keeps all five nondimensional numbers in equation (A7), i.e., with  $D_1 = \text{We}_s$ ,  $D_2 = \text{Ha}$ ,  $D_3 = G$ ,  $D_4 = \epsilon_s$  and  $D_5 = U_0$  one has Eq. (1) of the main text. However, specifying  $\nu$  based on a particular physical effect one recovers the various scalings employed in the literature:

(i) Using  $\nu = \epsilon^3 \gamma / \mu$  yields

$$D_1 = 1, \quad D_2 = \frac{\kappa L}{\epsilon \gamma}, \quad D_3 = \frac{\rho g L^2}{\gamma}, \quad D_4 = \frac{U_w \mu}{\epsilon^3 \gamma}, \quad D_5 = \frac{u \mu}{\epsilon^3 \gamma}. \quad (\text{A9})$$

With  $D_2 = 1$  (fixed by choosing  $L$ ),  $D_3 = G$ ,  $D_4 = 0$  and  $D_5 = U$  this corresponds to Eq. (1) of [22]. Note that there,  $\Pi(h)$  is made parameterless by choosing  $\delta$ . This corresponds to the case considered in the present section III [e.g., Fig. 3] where we keep  $\text{We}_s = 1$  and effectively recover the appropriate scaling.

(ii) Using  $\nu = U_w$  gives

$$D_1 = \frac{\epsilon^3 \gamma}{\mu U_w}, \quad D_2 = \frac{\epsilon \kappa \delta}{\mu U_w} = \text{Ha}, \quad D_3 = \frac{\epsilon \rho g \delta^2}{\mu U_w}, \quad D_4 = 1, \quad D_5 = \frac{u}{U_w}. \quad (\text{A10})$$

With  $D_2 = D_3 = D_5 = 0$  and  $D_1 = 1/\text{We}_s$  this corresponds to Eq. (2.23) of [43]. Note that there  $L$  and  $\delta$  are chosen by geometry and SAW-intrinsic length, respectively, and are not available to further reduce the count of dimensionless numbers. This corresponds to the case considered in the present section IV A and the begin of section IV B [Figs. 4, 5, and 9] as keeping  $\epsilon_s = 1$  we effectively recover the appropriate scaling. In Figs. 5 and 9 the additional effect of partial wettability is added.

(iii) Our work mainly shows that increasing the strength of SAW has an effect similar to increasing the plate velocity in [22]. However, we also want to retain the ability to study the influence of  $\text{We}_s$ , a parameter crucial in [43]. Using  $\nu = \epsilon \kappa \delta / \mu$  gives

$$D_1 = \frac{\epsilon^2 \gamma}{\kappa \delta} = \frac{1}{\text{We}_s}, \quad D_2 = 1, \quad D_3 = \frac{\rho g \delta}{\kappa} = G, \quad D_4 = \frac{\mu U_w}{\epsilon \kappa \delta} = \epsilon_s, \quad D_5 = \frac{\mu u}{\epsilon \kappa \delta} = U_0. \quad (\text{A11})$$

The lengths  $L$  and  $\delta$  are chosen as in [43]. This corresponds to the case considered in the main part of section IV B [Figs. 6-8 and 10-21] as keeping  $\text{Ha} = 1$  effectively implies this scaling. This allows for comparison with the behaviour in both limiting cases, i.e., Refs. [43] and [22], respectively.

- 
- [1] M. Abo Jabal, A. Egbaria, A. Zigelman, U. Thiele, and O. Manor. Connecting monotonic and oscillatory motions of the meniscus of a volatile polymer solution to the transport of polymer coils and deposit morphology. *Langmuir*, 34:11784–11794, 2018.
  - [2] E. L. Allgower and K. Georg. *Introduction to numerical continuation methods*, volume 45. SIAM, 2003.
  - [3] G. Altshuler and O. Manor. Spreading dynamics of a partially wetting water film atop a MHz substrate vibration. *Phys. Fluids*, 27:102103, 2015.
  - [4] G. Altshuler and O. Manor. Free films of a partially wetting liquid under the influence of a propagating MHz surface acoustic wave. *Phys. Fluids*, 28:072102, 2016.
  - [5] S. Alzuaga, J.-F. Manceau, and F. Bastien. Motion of droplets on solid surface using acoustic radiation pressure. *J. Sound Vib.*, 282:151–162, 2005.

- [6] J. Ashmore, A. Q. Shen, H. P. Kavehpour, H. A. Stone, and G. H. McKinley. Coating flows of non-Newtonian fluids: weakly and strongly elastic limits. *J. Eng. Math.*, 60:17–41, 2008.
- [7] D. Baratian, É. Ruiz-Gutiérrez, F. Mugele, and R. Ledesma-Aguilar. Slippery when wet: mobility regimes of confined drops in electrowetting. *Soft Matter*, 15:7063–7070, 2019.
- [8] A. L. Bertozzi, A. Münch, X. Fanton, and A. M. Cazabat. Contact line stability and ”undercompressive shocks” in driven thin film flow. *Phys. Rev. Lett.*, 81:5169–5173, 1998.
- [9] S. Biwersi, J. Manceau, and F. Bastien. Displacement of droplets and deformation of thin liquid layers using flexural vibrations of structures. influence of acoustic radiation pressure. *J. Acoust. Soc. Am.*, 107:661–664, 2000.
- [10] M. Bowen, J. Sur, A. L. Bertozzi, and R. P. Behringer. Nonlinear dynamics of two-dimensional undercompressive shocks. *Physica D*, 209:36–48, 2005.
- [11] F. P. Bretherton. The motion of long bubbles in tubes. *J. Fluid Mech.*, 10:166–188, 1961.
- [12] P. Carles and A. M. Cazabat. The thickness of surface-tension-gradient-driven spreading films. *J. Colloid Interf. Sci.*, 157:196–201, 1993.
- [13] M. S. Carvalho and H. S. Khesghi. Low-flow limit in slot coating: Theory and experiments. *AIChE Journal*, 46:1907–1917, 2000.
- [14] A. M. Cazabat, F. Heslot, S. M. Troian, and P. Carles. Fingering instability of thin spreading films driven by temperature gradients. *Nature*, 346:824–826, 1990.
- [15] R. V. Craster and O. K. Matar. Dynamics and stability of thin liquid films. *Rev. Mod. Phys.*, 81:1131–1198, 2009.
- [16] P.-G. De Gennes. Wetting: statics and dynamics. *Rev. Mod. Phys.*, 57:827, 1985.
- [17] B. V. Derjaguin. On the thickness of the liquid film adhering to the walls of a vessel after emptying. *Acta Physicochim. URSS*, 20:349–352, 1945.
- [18] B. V. Derjaguin. Untersuchungen des Spaltdruckes dünner Filme, deren Entwicklung, Ergebnisse und zu lösende aktuelle Probleme. *Colloid Polymer Sci.*, 253:492–499, 1975.
- [19] H. A. Dijkstra, F. W. Wubs, A. K. Cliffe, E. Doedel, I. F. Dragomirescu, B. Eckhardt, A. Y. Gelfgat, A. Hazel, V. Lucarini, A. G. Salinger, E. T. Phipps, J. Sanchez-Umbria, H. Schuttelaars, L. S. Tuckerman, and U. Thiele. Numerical bifurcation methods and their application to fluid dynamics: Analysis beyond simulation. *Commun. Comput. Phys.*, 15:1–45, 2014.
- [20] S. Engelnkemper, S. V. Gurevich, H. Uecker, D. Wetzel, and U. Thiele. Continuation for thin film hydrodynamics and related scalar problems. In A. Gelfgat, editor, *Computational Modeling of Bi-*

- furcations and Instabilities in Fluid Mechanics*, Computational Methods in Applied Sciences, vol 50, pages 459–501. Springer, 2019.
- [21] S. Engelnkemper, M. Wilczek, S. V. Gurevich, and U. Thiele. Morphological transitions of sliding drops - dynamics and bifurcations. *Phys. Rev. Fluids*, 1:073901, 2016.
  - [22] M. Galvagno, D. Tseluiko, H. Lopez, and U. Thiele. Continuous and discontinuous dynamic unbinding transitions in drawn film flow. *Phys. Rev. Lett.*, 112:137803, 2014.
  - [23] P. Gao, L. Li, J. J. Feng, H. Ding, and X. Y. Lu. Film deposition and transition on a partially wetting plate in dip coating. *J. Fluid Mech.*, 791:358–383, 2016.
  - [24] R. Goh and A. Scheel. Hopf bifurcation from fronts in the Cahn-Hilliard equation. *Arch. Ration. Mech. Anal.*, 217:1219–1263, 2015.
  - [25] M. Heil and A. L. Hazel. Oomph-lib - an object-oriented multi-physics finite-element library. In H.-J. Bungartz and M. Schäfer, editors, *Fluid-Structure Interaction: Modelling, Simulation, Optimisation*, pages 19–49. Springer Berlin Heidelberg, Berlin, Heidelberg, 2006.
  - [26] H. Ji, C. Falcon, A. Sadeghpour, Z. Zeng, Y. S. Ju, and A. L. Bertozzi. Dynamics of thin liquid films on vertical cylindrical fibres. *J. Fluid Mech.*, 865:303–327, 2019.
  - [27] B. Jin, A. Acrivos, and A. Münch. The drag-out problem in film coating. *Phys. Fluids*, 17:103603, 2005.
  - [28] M. H. Köpf, S. V. Gurevich, R. Friedrich, and L. Chi. Pattern formation in monolayer transfer systems with substrate-mediated condensation. *Langmuir*, 26:10444–10447, 2010.
  - [29] M. H. Köpf, S. V. Gurevich, R. Friedrich, and U. Thiele. Substrate-mediated pattern formation in monolayer transfer: a reduced model. *New J. Phys.*, 14:023016, 2012.
  - [30] M. H. Köpf and U. Thiele. Emergence of the bifurcation structure of a Langmuir-Blodgett transfer model. *Nonlinearity*, 27:2711–2734, 2014.
  - [31] M. T. Kreutzer, M. S. Shah, P. Parthiban, and S. A. Khan. Evolution of nonconformal Landau-Levich-Bretherton films of partially wetting liquids. *Phys. Rev. Fluids*, 3:014203, 2018.
  - [32] Y. A. Kuznetsov. *Elements of Applied Bifurcation Theory*, volume 112. Springer, New York, 3rd edition, 2010.
  - [33] L. Landau and B. Levich. Dragging of a liquid by a moving plane. *Acta Physicochim. URSS*, 17:42, 1942. reprinted in [49], p. 141–151.
  - [34] V. Lapuerta, F. J. Mancebo, and J. M. Vega. Control of Rayleigh-Taylor instability by vertical vibration in large aspect ratio containers. *Phys. Rev. E*, 64:016318, 2001.

- [35] T.-S. Lin, S. Rogers, D. Tseluiko, and U. Thiele. Bifurcation analysis of the behavior of partially wetting liquids on a rotating cylinder. *Phys. Fluids*, 28:082102, 2016.
- [36] T. S. Lin, D. Tseluiko, M. G. Blyth, and S. Kalliadasis. Continuation methods for time-periodic travelling-wave solutions to evolution equations. *Appl. Math. Lett.*, 86:291–297, 2018.
- [37] P.-M. T. Ly, K. D. J. Mitas, U. Thiele, and S. V. Gurevich. Two-dimensional patterns in dip coating - first steps on the continuation path. *Physica D*, 409:132485, 2020.
- [38] P.-M. T. Ly, U. Thiele, L. Chi, and S. V. Gurevich. Effects of time-periodic forcing in a Cahn-Hilliard model for Langmuir-Blodgett transfer. *Phys. Rev. E*, 99:062212, 2019.
- [39] Y.-P. Ma, J. Burke, and E. Knobloch. Defect-mediated snaking: A new growth mechanism for localized structures. *Physica D*, 239:1867–1883, 2010.
- [40] M. Maleki, M. Reyssat, F. Restagno, D. Quéré, and C. Clanet. Landau-Levich menisci. *J. Colloid Interf. Sci.*, 354:359–363, 2011.
- [41] O. Manor, A. R. Rezk, J. R. Friend, and L. Y. Yeo. Dynamics of liquid films exposed to high-frequency surface vibration. *Phys. Rev. E*, 91:053015, 2015.
- [42] S. Mhatre, A. Zigelman, L. Abezgauz, and O. Manor. Influence of a propagating megahertz surface acoustic wave on the pattern deposition of solute mass off an evaporating solution. *Langmuir*, 32:9611–9618, 2016.
- [43] M. Morozov and O. Manor. An extended Landau-Levich model for the dragging of a thin liquid film with a propagating surface acoustic wave. *J. Fluid Mech.*, 810:307–322, 2017.
- [44] M. Morozov and O. Manor. Vibration-driven mass transfer and dynamic wetting. *Curr. Opin. Colloid Interf. Sci.*, 36:37–45, 2018.
- [45] A. Münch. Pinch-off transition in Marangoni-driven thin films. *Phys. Rev. Lett.*, 91:016105, 2003.
- [46] A. Münch and P. L. Evans. Marangoni-driven liquid films rising out of a meniscus onto a nearly-horizontal substrate. *Physica D*, 209:164–177, 2005.
- [47] A. Oron, S. H. Davis, and S. G. Bankoff. Long-scale evolution of thin liquid films. *Rev. Mod. Phys.*, 69:931–980, 1997.
- [48] A. O. Parry, C. Rascon, E. A. G. Jamie, and D. G. A. L. Aarts. Capillary emptying and short-range wetting. *Phys. Rev. Lett.*, 108:246101, 2012.
- [49] P. Pelce, editor. *Dynamics of curved fronts*. Academic Press, London, 1988.
- [50] L. M. Pismen. Nonlocal diffuse interface theory of thin films and the moving contact line. *Phys. Rev. E*, 64:021603, 2001.

- [51] T. D. Reynolds, S. K. Kalpathy, S. Kumar, and L. F. Francis. Dip coating of charged colloidal suspensions onto substrates with patterned wettability: coating regime maps. *J. Colloid Interf. Sci.*, 352:202–210, 2010.
- [52] A. R. Rezk, O. Manor, J. R. Friend, and L. Y. Yeo. Unique fingering instabilities and soliton-like wave propagation in thin acoustowetting films. *Nat. Commun.*, 3:1167, 2012.
- [53] A. R. Rezk, O. Manor, L. Y. Yeo, and J. R. Friend. Double flow reversal in thin liquid films driven by megahertz-order surface vibration. *Proc. R. Soc. A*, 470:20130765, 2014.
- [54] B. Scheid, J. Delacotte, B. Dollet, E. Rio, F. Restagno, E. A. van Nierop, I. Cantat, D. Langevin, and H. A. Stone. The role of surface rheology in liquid film formation. *Europhys. Lett.*, 90:24002, 2010.
- [55] M. Schneemilch and A. M. Cazabat. Wetting films in thermal gradients. *Langmuir*, 16:8796–8801, 2000.
- [56] J. Snoeijer, B. Andreotti, G. Delon, and M. Fermigier. Relaxation of a dewetting contact line. part 1. a full-scale hydrodynamic calculation. *J. Fluid Mech.*, 579:63–83, 2007.
- [57] A. Staicu and F. Mugele. Electrowetting-induced oil film entrapment and instability. *Phys. Rev. Lett.*, 97:167801, 2006.
- [58] V. M. Starov and M. G. Velarde. Surface forces and wetting phenomena. *J. Phys.-Condens. Matter*, 21:464121, 2009.
- [59] W. Tewes, M. Wilczek, S. V. Gurevich, and U. Thiele. Self-organised dip-coating patterns of simple, partially wetting, nonvolatile liquids. *Phys. Rev. Fluids*, 4:123903, 2019.
- [60] U. Thiele. Structure formation in thin liquid films. In S. Kalliadasis and U. Thiele, editors, *Thin Films of Soft Matter*, pages 25–93, Wien, 2007. Springer.
- [61] U. Thiele. Thin film evolution equations from (evaporating) dewetting liquid layers to epitaxial growth. *J. Phys.-Condens. Matter*, 22:084019, 2010.
- [62] U. Thiele. Patterned deposition at moving contact line. *Adv. Colloid Interf. Sci.*, 206:399–413, 2014.
- [63] U. Thiele. Recent advances in and future challenges for mesoscopic hydrodynamic modelling of complex wetting. *Colloids Surf. A*, 553:487–495, 2018.
- [64] U. Thiele, T. Frohoff-Hülsmann, S. Engelinkemper, E. Knobloch, and A. J. Archer. First order phase transitions and the thermodynamic limit. *New J. Phys.*, 21:123021, 2019.
- [65] U. Thiele, J. M. Vega, and E. Knobloch. Long-wave Marangoni instability with vibration. *J. Fluid Mech.*, 546:61–87, 2006.
- [66] S. Trinschek, F. Stegemerten, K. John, and U. Thiele. Thin-film modelling of resting and moving



- active droplets. *Phys. Rev. E*, x:x, 2020. (at press).
- [67] D. Tseluiko, M. Galvagno, and U. Thiele. Collapsed heteroclinic snaking near a heteroclinic chain in dragged meniscus problems. *Eur. Phys. J. E*, 37:33, 2014.
  - [68] H. Uecker. Hopf bifurcation and time-periodic orbits with pde2path algorithms and applications. *Commun. Comput. Phys.*, 25, 2017.
  - [69] H. Uecker. Steady bifurcations of higher multiplicity in pde2path. 2018.
  - [70] H. Uecker, D. Wetzel, and J. D. M. Rademacher. pde2path-A Mat lab Package for Continuation and Bifurcation in 2d Elliptic Systems. *Numer. Math.-Theory, Methods Appl.*, 7:58–106, 2014.
  - [71] S. J. Weinstein and K. J. Ruschak. Coating flows. *Annu. Rev. Fluid Mech.*, 36:29–53, 2004.
  - [72] M. Wilczek, W. B. H. Tewes, S. V. Gurevich, M. H. Köpf, L. Chi, and U. Thiele. Modelling pattern formation in dip-coating experiments. *Math. Model. Nat. Phenom.*, 10:44–60, 2015.
  - [73] M. Wilczek, J. Zhu, L. Chi, U. Thiele, and S. V. Gurevich. Dip-coating with prestructured substrates: transfer of simple liquids and Langmuir–blodgett monolayers. *J. Phys.-Condens. Matter*, 29:014002, 2016.
  - [74] J. Zhu, M. Wilczek, M. Hirtz, J. Hao, W. Wang, H. Fuchs, S. V. Gurevich, and L. Chi. Branch suppression and orientation control of Langmuir–Blodgett patterning on prestructured surfaces. *Adv. Mater. Interf.*, 3:1600478, 2016.
  - [75] J. Ziegler, J. H. Snoeijer, and J. Eggers. Film transitions of receding contact lines. *Eur. Phys. J.-Spec. Top.*, 166:177–180, 2009.